Glacial Isostatic Adjustment Modelling of the Coast Mountains of British Columbia

by

Maximilian Lauch
B.Sc., McMaster University, 2017

A Thesis Submitted in Partial Fulfillment of the
requirements for the Degree of

MASTER OF SCIENCE

in the School of Earth and Ocean Sciences

We acknowledge and respect the lək̓ʷəŋən peoples on whose traditional territory the university stands and the Songhees, Esquimalt and W̱SÁNEĆ peoples whose historical relationships with the land continue to this day.

Glacial Isostatic Adjustment Modelling of the Coast Mountains of British Columbia

by

Maximilian Lauch
B.Sc., McMaster University, 2017

Supervisory Committee

Dr. Thomas S. James, Co-supervisor (School of Earth and Ocean Sciences)

Dr. Lucinda Leonard, Co-supervisor (School of Earth and Ocean Sciences)

Dr. Yan Jiang, Committee Member (School of Earth and Ocean Sciences)

Abstract

The Coast Mountains in British Columbia contain over 10,000 km^2 of glacial ice. While these glaciers have lost significant mass since the Little Ice Age (LIA; around 300 years before present), the melting rate has significantly increased over the past decade, likely due to the effects of climate change. The purpose of this study was to develop an approach to quantifying the isostatic response to LIA glacier change and investigate how it can further our understanding of the Earth's rheology through GIA modelling. The Coast Mountains in southwestern British Columbia were chosen due to their significant ice mass loss since the LIA, their location in a tectonically active region, which includes a volcanic arc, and the presence of information of vertical land motion.

The GIA models in this study use a wide range of Earth rheological parameters that are then constrained through comparison to observations of vertical land motion in the region. The study used available Global Navigation Satellite System (GNSS) vertical velocity data as the observable from seven GNSS sites in southwestern BC, using a combination of Western Canada Deformation Array (WCDA) and British Columbia Active Control System (BCACS) GNSS stations. Raw data were analyzed using the GIPSY 6.4 software following the Precise Point Positioning processing strategy.

Two ice load histories were developed based on gridded estimates of present-day ice thicknesses in the region in order to simulate the change in the surface loading as the glacial ice mass fluctuates over time. Ice Load A used a simple uniform thickness change profile over 3 time-steps based on extrapolated modern melt rates. Ice Load B is more complex and utilized a published profile of glacier change through time basing the magnitude of volume changes on the volume-area scaling relationship with a range of coefficient values. This allowed for a range of ice change magnitudes to be tested. The Earth models used were spherically symmetric Preliminary Reference Earth Models (PREM). Their viscosity structure is based on VM5a for the transition zone and lower mantle, but with variable lithospheric thickness and

asthenospheric viscosity. The goodness of fit for the modeled velocities were compared to the observed velocities using a normalized RMS (NRMS) statistic. Ice Load A models had a best fitting lithospheric thickness of 50 km and an asthenospheric viscosity of 2×10^{19} Pa s. For all variations of Ice Load B, the best fitting model parameters had lithospheric thicknesses ranging from 45 km to 55 km and asthenospheric viscosities between 6×10^{18} Pa s and 3×10^{19} Pa s. Corrected GNSS vertical velocity observations were tested to check the effects of interseismic vertical signal and assumed residual GIA from the Cordilleran Ice Sheet. However, the corrections did not improve the NRMS fit. Overall, the asthenospheric viscosity results from this study overlap with all the ranges found in the previous studies while lithospheric thicknesses agree with some past studies.

The results of this study generally align with previous work and the current understanding of the Coast Mountains region and can inform a future round of sea-level projections for the region as ice mass loss continues in the Coast Mountains. This study serves to further refine constraints on Earth rheology and can be used to guide future work on GIA in the region.

Table of Contents

List of Tables

List of Figures

Acknowledgments

I have received a great deal of guidance and support from many people during the duration of completing this Master's thesis.

I would like to first thank my supervisors, Dr. Thomas James and Dr. Lucinda Leonard. Tom, your unwavering support, and patience were invaluable to the completion of this project. Thank you for your scientific and technical expertise. Lucinda, thank you for your thoughtful feedback and for providing me with field work opportunities to enhance my Master's experience.

To my committee member Dr. Yan Jiang, thank you for providing me with the integral datasets and instruction necessary to complete this thesis. Thank you to Dr. Joe Henton for the one-on-one video calls on analyzing the GNSS time-series. Additionally, I would like to thank both Dr. Brian Menounos for personally providing your glaciology advice and data and Dr. Maryam Yousefi for sharing your interseismic deformation model results.

I would like to acknowledge the Generic Mapping Tool (GMT) by Wessel and Smith which was used for the contour and study area mapping. I would also like to acknowledge the spark V2 program by Simon Banville from the Canadian Geodetic Survey that was used to analyze the GNSS time-series and generate the time-series graphs.

Finally, thank you to my mother, father, and sister for constant emotional and academic support, and for sharing your experiences and editing expertise. To my Oma and Opa, thank you for your check-in phone calls and constant words of wisdom. To my friends and partner (Jen) thank you for the support and encouraging the casual break for libations and culinary adventures.

Chapter 1: Introduction

1.1 Overview

The Coast Mountains of British Columbia include about 10,900 km^2 of glacial ice, mountain peaks as high as 4000 m, and active volcanoes (Schiefer *et al*., 2007). The topography of the region has been built up through millions of years of tectonics and volcanism and then shaped by dramatic glacial events, including being covered by the massive Cordilleran Ice Sheet at the Last Glacial Maximum. In this study, the focus is on the central and southern portions of the Coast Mountains. The Central Coast Mountains (CCM) lie between 52° N and 56° N, while the Southern Coast Mountains (SCM) lie between 47° N and 52° N. The SCM lie in the volcanic arc and adjacent regions of the Cascadia Subduction Zone (CSZ), where the Juan de Fuca plate is subducting under the North America plate. The CCM are located east of a major transform fault called the Queen Charlotte Fault (Figure 1.1). Due to the extensive history of

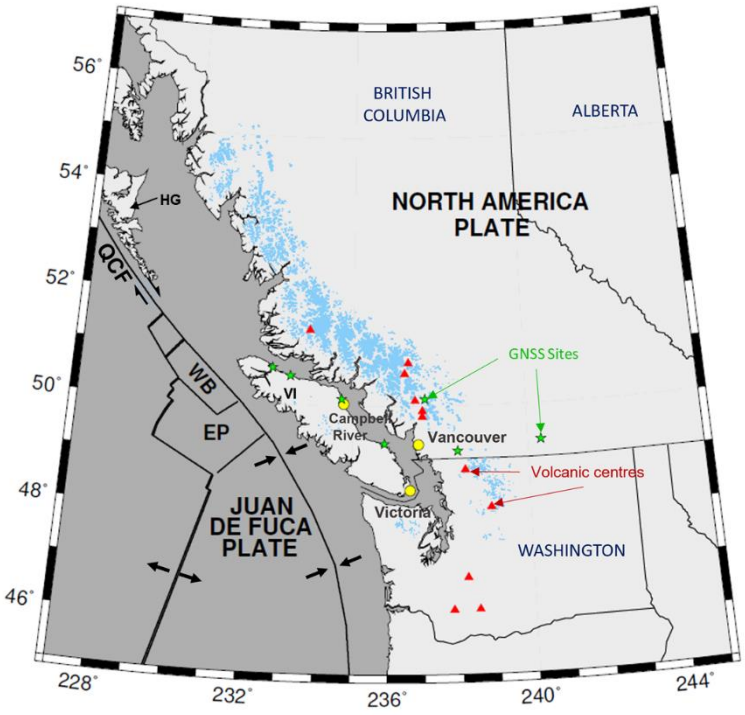

Figure 1.1: *The study area consists of the Southern Coast Mountains (about 47° N to 52° N) and the central Coast Mountains (about 52° N to 56° N). Red triangles indicate volcanic centres of the Coast Range Volcanic arc. EP is the Explorer plate, WB is the Winona block, QCF is the Queen Charlotte Fault, HG is Haida Gwaii, and VI is Vancouver Island. Green stars are GNSS sites used in this study, and yellow circles are selected metropolitan centres.*

glacial fluctuations, the Coast Mountains have undergone and are undergoing glacial isostatic adjustment (GIA). The region is experiencing active tectonics and volcanism, in contrast to the much older, and stable, North American craton, further to the east.

This chapter provides background to the region and a review of previous work on GIA modelling in the region, which provides constraints on Earth rheology. The following sections describe the tectonic history, glacial history, modern glacial change, glacial isostatic adjustment, and GIA modelling in the Coast Mountain region, respectively.

1.2 Tectonic History

The present topography of the Coast Mountains began to take shape in the Cretaceous period, in what is known as the Coast Range Episode (Mathews, 1991). Spreading from the Pacific-Farallon Ridge, the oceanic Farallon plate converged and subducted under the continental North America plate. As the Farallon plate subducted beneath the North America plate, it carried several crustal units (known as terranes) that collided and subsequently accreted to the western edge of the North America plate. As a result, the western North America plate presently consists of 5 accreted terranes, now known as morpho-geological belts (Figure 1.2).

The Coast Range Episode occurred when the Insular terrane collided with the Intermontane Belt of the North America plate. The subduction of the Insular terrane under the Intermontane belt eventually stopped and the Insular terrane accreted to the North America plate (Mathews, 1991). The collision and accretion of the Insular terrane, along with the continued subduction of the Farallon plate beneath the now expanded North America plate, caused the growth of the Coast Mountains through orogeny and the intrusion of molten rock to form the Coast Range Volcanic Arc, of which the Garibaldi Volcanic Arc is a part (Church and Ryder, 2010). The Farallon plate would eventually break apart, and the remnant portion that is now subducting beneath North America at the CSZ is known as the Juan de Fuca plate

(Figure 1.1).

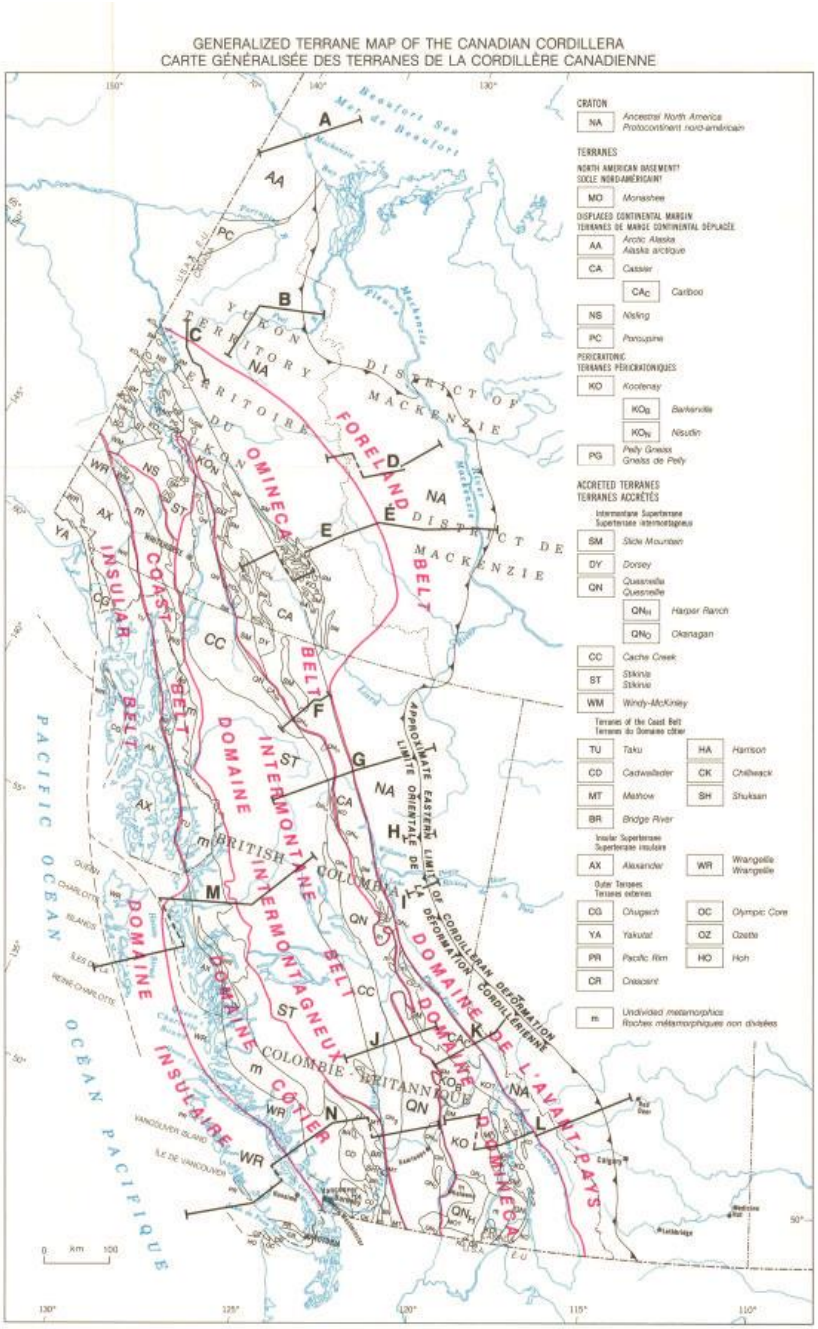

Figure 1.2: *Morpho-geological make up of western Canada showing the belts (formerly terranes) that accreted to the North America plate (Gabrielse, 1991).*

The majority of mountain building took place during this period, but the crustal uplift continued, raising mountain peak heights to about 2500 m above present sea level by the end of the Miocene (Mathews, 1991). Another period of intense uplift followed in the past 10 million years, raising the mountains to

the elevations we see today, up to 4000 m above sea level (Church and Ryder, 2010).

The area is a region of present-day active tectonics. The movements of the Pacific plate, North America plate, and Juan de Fuca and Explorer plates control the region's tectonics. A triple junction is located north of Vancouver Island and south of Haida Gwaii, and a major right-lateral transform fault is located west of Haida Gwaii (Church and Ryder, 2010). While the tectonic history and setting are vital to understanding the geological framework of the Coast Mountains, tectonics alone did not determine their present-day configuration and topography. The following section outlines how the landscape today was influenced by glacial cycles.

1.3 Glacial History

Glaciers in the Coast Mountains began as alpine formations that grew among the mountains and higher elevation terrains (Clague *et al*., 1989). They grew and periodically expanded out of the mountains during glacial periods, even coalescing and forming a continental ice sheet, such as the Cordilleran Ice Sheet that formed during the Fraser Glaciation. There is evidence of glaciation as far back as the late Tertiary period and early Pleistocene (about 3 - 2.5 Ma) with glacial till interbedded with lava flows (Clague *et al*., 1989). Evidence for glaciation is more robust within the following Quaternary period. The Quaternary period began about 2.5 million years before the present (2.5 Ma) and extends to the present day. During this time, there were glacial and interglacial periods during which the Quaternary Coast Mountain glaciers fluctuated in advances and retreats.

1.3.1 Fraser Glaciation

The Fraser Glaciation is the most recent glacial period in this region. The Fraser Glaciation began as early as 29 ka and ended around 13-9 ka. The Fraser glaciation had 3 phases: (i) Ice Expansion Phase, (ii) Maximum Phase, and (iii) Late Glacial Phase (Stumpf *et al.*, 2000).

I. Ice Expansion Phase

Prior to 30 ka, ice slowly accumulated and fluctuated in extent in the high elevation regions of the Coast

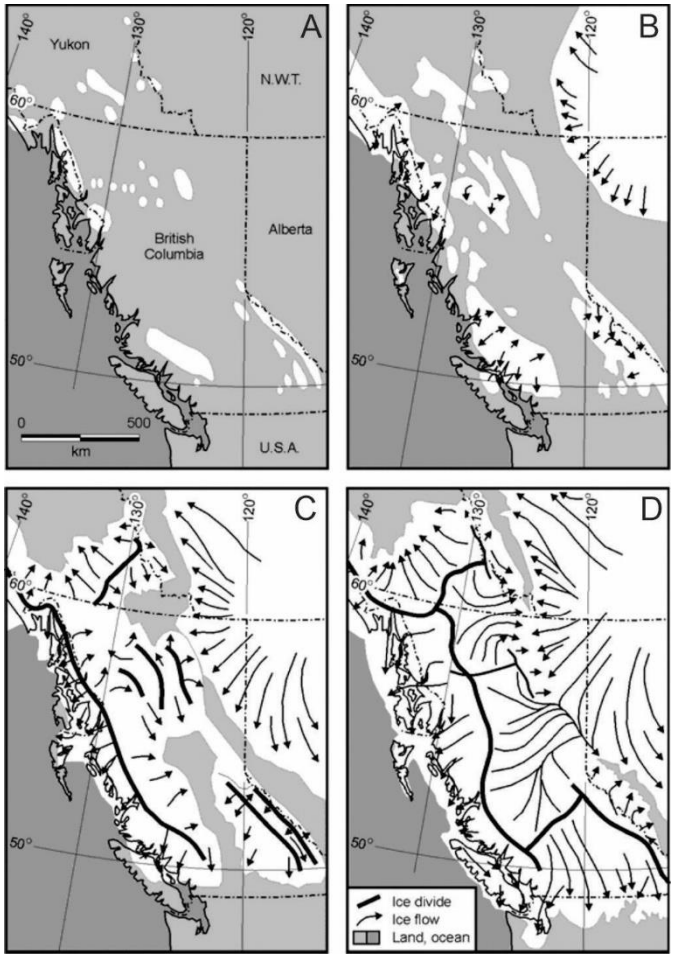

Figure 1.3: *Map of ice flow direction in the Coast Mountain regions during the Fraser Glaciation: (A) 35 ka, (B) 30 ka, (C) 25 ka, and (D) 18 ka (Clague and Ward, 2011).*

Mountains (Figure 1.3A)(Clague and Ward, 2011). Beginning around 29 ka, ice accumulation increased in the small mountain icefields as the climate continued to cool and precipitation increased, slowly growing the alpine ice masses (Figure 1.3B). Around 25 ka, they grew sufficiently to advance out of the mountains and flow into the valleys and lowlands of the surrounding landscapes (Stumpf *et al.*, 2000). The ice advanced across plateaus and into the lowlands of the interior and Pacific coast. Glaciers accumulated during this period to the point that they reached a large enough thickness to flow over mountains and reached above 1700 metres above sea level (m asl). Valley glaciers integrated and formed piedmont or plateau ice sheets (Stumpf *et al.*, 2000). During this phase, the mountainous zones

remained the principal sources of ice accumulation (Figure 1.3C). Accumulation zones remained in the mountains during this period. Ice thickness and mass were not enough to overcome topography controls, and ice flow was mainly within valleys, fjords, and downslope directions (Clague and Ward, 2011).

II. Maximum Phase

The Maximum Phase occurred between 18 and 14 ka, and is when the continental ice sheet formed (Stumpf *et al*., 2000). Accumulation continued for the piedmont and plateau ice sheets until they eventually coalesced to form one continuous sheet, the Cordilleran Ice Sheet. Ice thickened to the extent where ice domes were formed over the interior. Accumulation centres shifted towards these interior domes, and the ice sheet would eventually reach its climactic maximum size (Figure 1.3D). As

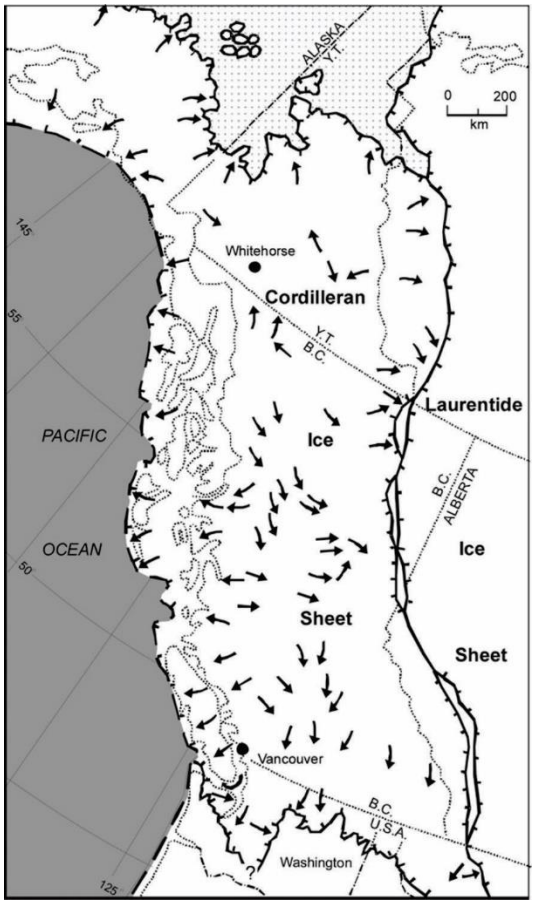

Figure 1.4: *Maximum extent of Cordilleran Ice Sheet around 17 ka, arrows indicate direction of ice flow (Clague and Ward, 2011)*

wide as 900 km, the Cordilleran Ice Sheet reached east to the Laurentide Ice sheet and westward over the continental shelf margin, covering present coastal islands, shown in Figure 1.4 (Darvill *et al*., 2018; Barrie and Conway, 1999). At this maximum size, the ice sheet obtained a surface elevation of 2000-3000 m asl (above present sea level), enveloping the lower relief topography while also flowing upslope over some mountains to the west, no longer confined by bedrock topographic controls (Figure 1.5A) (Stumpf *et al*., 2000). The ice sheet reached thicknesses of more than 2000 m over major valleys (Ryder *et al*., 1991).

III. Late Glacial Phase

Beginning around 13 ka, the Cordilleran Ice Sheet rapidly declined in size until about 9 ka, where the ice coverage in the Coast Mountains returned to pre-Fraser levels, similar to the coverage seen today (Church and Ryder, 2010). Deglaciation occurred in the form of complex frontal retreat in the periphery of the ice sheet and from rapid down wasting (Clague and Ward, 2011). As the climate warmed, the interior ice began to stagnate across the domes of the ice sheet. Accumulation centres that had previously shifted from the mountains to the interior began to reverse and return to their previous alpine positions (Stumpf *et al.*, 2000). Glacier flow continued in the Coast Mountains during this period, continuing to flow westward to the Pacific Ocean through low elevation mountain passes. It was not until the ice surface elevation decayed to less than around 1500 m asl (Figure 1.5B), lower than the elevation of these mountain passes, that the ice flow halted and sometimes even reversed back towards the interior, no longer able to overcome topographic controls and to flow downslope once again (Stumpf *et al.*, 2000). The western portion was rapidly freed of ice coverage as the lobes calved back to valleys and fjord heads, leaving behind stagnant, dead ice in the lower elevation valleys (Figure 1.5C).

1.3.2 Late Pleistocene (14 – 11 ka)

The final phases of the Cordilleran Ice Sheet were not characterized by uniform thinning and retreat, but rather retreat was interrupted by more minor advances that were not synchronous across all regions

(Schiefer *et al.*, 2007; VanLooy and Forster, 2008; Koch *et al.,* 2009). These smaller periods of advance could have occurred from rapid climatic cooling events, non-climatic causes such as the sea-level change from the large-scale melting across the continental sheet, or simply from topographic effects (Menounos *et al*., 2009). The alpine glaciers experienced three main advance periods during the last 3000 years of the Pleistocene. The last took place around 11.5 ka and is referred to as the Younger Dryas Chronozone. It generated a temporary stillstand that punctuated the thinning and retreat of the Cordilleran Ice Sheet (Menounos *et al*., 2009; Schiefer *et al*., 2007).

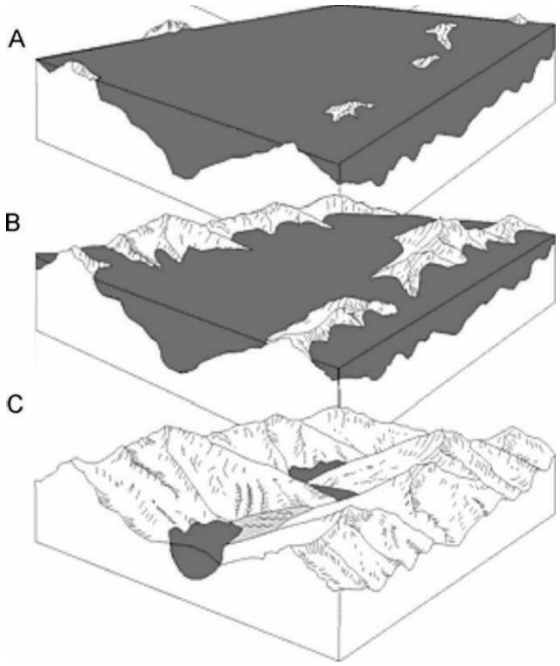

Figure 1.5*: The Late Glacial Phase deglaciation can be broken down into 3 subphases: (A) end of maximum phase, at the turning point where deglaciation begins, (B) where the ice sheet begins to downwaste and lose elevation and stagnates, and (C) where the ice accumulation has retreated back to the mountains and calved ice remains dead in the valleys (Clague and Ward, 2011).*

1.3.3 Early Holocene (11 – 7.5 ka)

Most evidence points to early Holocene glaciers in the Coast Mountains being more restricted than their modern counterparts (Menounos *et al*., 2009). A silty interval in a core collected from lower Joffre Lake in the SCM suggests a minor glacier advance between 10.15 and 7.51 ka. Detrital wood found in deglaciated areas at the forefield of Sphinx and Sentinel glaciers further indicate an advance in this

period, synchronous with the 8200-year cold event in the North Atlantic (Menounos *et al*., 2004; Menounos *et al*., 2009).

1.3.4 Neoglaciation (7.5 – 1 ka)

Recent glacial retreat has exposed wood samples that are evidence of glacial advances from 7.5 to 1 ka. The first has been characterized as the "Garibaldi Phase" due to much of the evidence coming from Garibaldi Provincial Park in the SCM. The Garibaldi phase occurred between 6.95 and 5.62 ka (Ryder and Thomson, 1986; Menounos *et al*., 2009). Another two glacial advances occurred between 5 and 3.5 ka. Evidence for these advances was found by analyzing detrital wood samples in till, again in Garibaldi Provincial Park (Koch *et al.*, 2007).

Finally, three more advances have been noted in the Southern Coast Mountains during this period. The first two occurred sometime during the "Tiedemann Advance" between 3.3 and 1.9 ka (Ryder and Thomson, 1986). The third and final Neoglaciation advance occurred during the period known as the "First Millennium Advance" between 1.6 and 1.3 ka (Menounos *et al*., 2009).

1.3.5 Little Ice Age

For the Coast Mountains, the Little Ice Age (LIA) has been defined as encompassing the glacier advances of the past millennium (Menounos *et al*., 2009). The LIA advances began around the 12th and 13th centuries, reaching maximum extents between the 17th and 19th centuries and ending as late as the 20th century. The LIA maximums are often characterized as the most extensive advancements since the end of the Fraser Glaciation (Clague *et al*., 2009; Menounos *et al*., 2009). The LIA advances are largely synchronous across the Coast Mountains, Alaska, and Patagonia.

In the CCM, Desloges and Ryder (1990) performed carbon dating of detritus samples from end moraines of 16 glaciers around the Monarch Icefield (in the Bella Coola area). The authors found that most terminal moraines date from 1860 to 1900, with some recessional moraines between 1900 and 1940 (Desloges and Ryder, 1990).

Figure 1.6: Relative glacier extent for Garibaldi Park Glaciers compared to three glaciers in the European Alps during the Little Ice Age (Koch et al., 2007a).

Studies of the SCM indicate that the Neoglacial history is in good agreement with the dates from the CCM, with some indication that the more southern glaciers advanced to their maximum earlier, with later, lesser, advances occurring at the end of the 19th century. Koch *et al.* (2007) describe the LIA history of nine glaciers in Garibaldi Provincial Park. The authors found that all nine glaciers have clear LIA terminal moraines dated to between 1690 and 1720 (Koch *et al*., 2007a). Koch *et al.* (2009) reconstructed the fluctuations of the Garibaldi Provincial Park glaciers using historical documents, aerial photographs, and dendrochronological samples from moraines and till. Over 505 km^2 of ice covered the park at the beginning of the 18th century, with only 49% remaining by 1987-1988 (Koch *et al*., 2009).

Following the Little Ice Age, the glaciers of the Coast Mountains have largely seen widespread decay due to climatic fluctuations and, more recently, anthropogenic climate change. Quantifying this increased melting since the LIA is achieved using a combination of dendrochronology, geomatics, and remote sensing, as described in the next section.

1.4 Modern Glacial Change

Schiefer *et al.* (2007) measured the volume loss across all British Columbia glaciers from 1985 to 1999 by comparing the Shuttle Radar Topography Mission (SRTM) digital elevation model (DEM) data from 1999 and digital terrain models made from aerial photography taken between 1982 and 1988. By comparing and aligning both DEMs, it was possible to see glacier elevation changes within the time interval and then calculate volume change based on these elevation changes and glacier extent, and from that discern a melt rate (Table 1.1) (Schiefer *et al.*, 2007). An average melt rate of -0.89 ± 0.23 m yr^{-1} (expressed as an ice thickness change) was calculated over this period for the SCM, and -0.61 ± 0.16 m yr^{-1} for the CCM.

From the same SRTM and digital terrain models, VanLooy and Forster (2008) analyzed datasets from five specific icefields in the SCM, with some corrections applied for elevation errors. The five icefields

selected were the Monarch, Ha-Iltzuk, Mount Waddington, Homathko, and Lillooet icefields. Table 1.1 shows the measured values for ice area, volume change, and area-averaged thinning rate for these icefields between the mid-1980s and 1999. Additionally, measurements were taken of the icefield terminus retreat rates over three time periods, from the aerial photography in the 1980s and a survey taken in 1926 (VanLooy and Forster, 2008).

In another study, Koch *et al.* (2009) examined thirteen glaciers in Garibaldi Provincial Park, again using the SRTM from 1999 with the photographs from the 1980s, along with the previously mentioned photographs from the survey in 1926. Following the same approach as VanLooy and Forster (2008), Koch *et al.* measured the ice area, volume change, thinning rate, and elevation change for 45 individual glaciers in Garibaldi Provincial Park. Table 1.1 shows the results for the 5 glaciers with the largest area. Koch *et al.* (2009) also created the first digitized topographic map of the area from these 1926 photographs. They then produced 25 m DEMs after georeferencing and correcting for elevation errors with the 1980 aerial survey. Glacier extents were mapped from a Landsat Thematic Mapper satellite image taken in 2005 in order to compare the extents to the earlier data sets. An example of this comparison can be seen in Figure 1.6, showing the extent of Sentinel Glacier from its LIA maximum to the 2005 extent, showing the extent in 1928, 1949, 1969, and 1977 (Koch *et al.*, 2009).

As can be seen in Table 1.1 the volume changes vary between the studies, but this is also associated with the different glacier areas. For example, the volume changes from VanLooy and Forster (2008) refer to total volume change per year for entire icefields, while Koch *et al*. (2009) have total volume changes per year for individual glaciers, which are several orders of magnitude smaller.

Results from these studies comparing the Coast Mountain glaciers between the mid-1980s and 1999 found relative synchronicity in the melting of the SCM glaciers. They all concluded that deglaciation has been occurring relatively consistently since at least 1928, although some glaciers did experience

localized advances, particularly within Garibaldi Park.

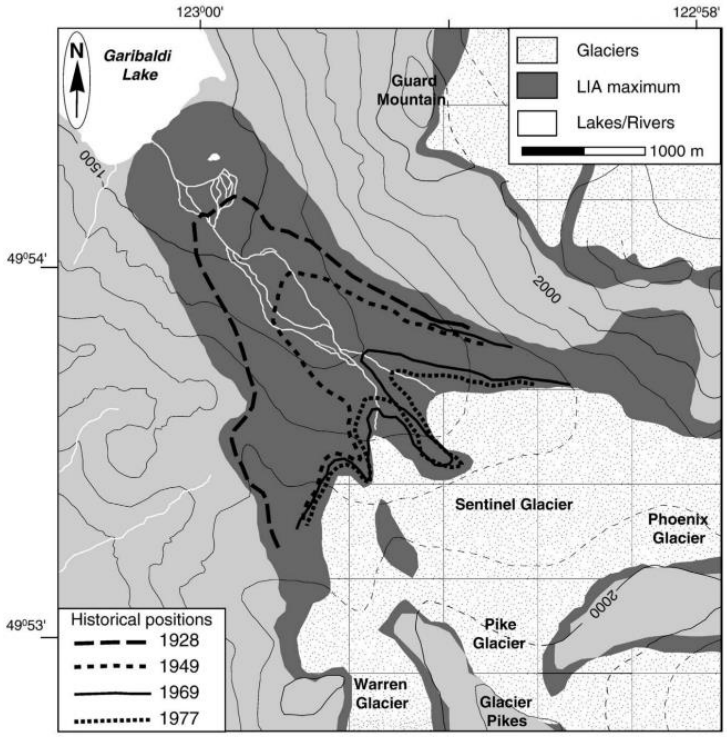

Figure 1.6*: Extent of Sentinel Glacier over time. Dark gray represents the LIA maximum extent. Black lines represent different historical positions (Koch* et al*., 2007).*

Table 1.1: Comparison of 3 studies done on Southern Coast Mountain glacier changes between the mid 1980s and 1999

Study Area	**Ice Area (km^2)**	**Volume Change ($km^3 a^{-1}$)**	**Thinning Rate ($m a^{-1}$)**	**Elevation Change (m)**
Schiefer *et al.,* 2007 (data from 1985-1999)				
S. Coast Mountains	8037	-7.13 ± 1.82	-0.89 ± 0.23	N/A
VanLooy and Forster, 2008 (data from 1984-1999)				
Monarch Icefield	491	-0.22 ± 0.12	-0.4 ± 0.2	N/A
Ha-Iltzuk	854	-0.85 ± 0.14	-1.0 ± 0.2	N/A
Mount Waddington	701	-0.15 ± 0.14	-0.2 ± 0.2	N/A
Homathko	569	-0.17 ± 0.13	-0.3 ± 0.3	N/A
Lillooet	603	-0.09 ± 0.15	-0.2 ± 0.3	N/A
Koch *et al.* 2009 (data from 1987-1999)				
Cheakamus	7.90	-0.001 ± 0.003	-0.92	-11.00
Lava/Bishop	6.37	-0.008 ± 0.002	-1.25	-15.00

Weart	10.17	-0.011 ± 0.003	-1.08	-13.00
Warren	5.23	-0.005 ± 0.002	-1.00	-12.00
Macbride	6.06	-0.004 ± 0.002	-0.67	-8.00

Cryosat-2 is a European Space Agency (ESA) satellite used to measure properties of global ice, including thickness and elevation. Altimetry data collected on the Southern Coast Mountains from 2010 to 2016 were used to determine elevation changes of glacier ice over the study period to measure how the glaciers grew or melted (Gower, 2017). The Cryosat-2 data showed a definite widespread melting trend in the area, with an absence of growth in ice over 2000 m asl. Melt rates were measured up to 2 metres per year (an elevation change of -2 m yr^{-1}) (Gower, 2017). The Cryosat project has proven to be a valuable tool in remotely monitoring alpine ice melt through interferometric radar altimetry measurements over time.

Another helpful tool for measuring ice mass-balance is the Gravity Recovery and Climate Experiment mission (GRACE). The GRACE mission used two satellites orbiting in tandem while measuring changes in speed and distance between them to create a mapping of static and time-variable gravity (Luthcke *et al*., 2008). GRACE data were used to measure glacier mass-balance changes over 10-day periods with a resolution of 2 x 2 degrees in Alaska between 2003 and 2007 (Luthcke *et al*., 2008). Jiang *et al.* (2021) combine GRACE with other geodetic observation methods in a global inversion to separate surface mass changes from GIA. GRACE data are used to track surface mass trends as well as subsurface mass changes caused by GIA. Notable present-day changes to ice masses were found in the Gulf of Alaska and Patagonia.

Menounos *et al.* (2018) used surface elevation change data from Advanced Spaceborne Thermal Emission, and Reflection Radiometer (ASTER) surveys to quantify ice elevation change during the survey period. The authors analyzed ASTER data over western North American glaciers, excluding Alaska, for

two main periods: 2000-2009 and 2009-2018. They found that, on average, the glaciers in their study region lost more than four times the ice mass in the later period (-12.3 ± 4.6 Gt yr^{-1} in 2009-2018) than in the earlier period (-2.9 ± 3.1 Gt yr^{-1} in 2000-2009).

The cycles of glacial growth and decay described in section 1.3, as well as the modern glacial ice mass loss described here, lead to changes in the ice load exerted on the underlying Earth. The isostatic responses of the Earth to these load changes are described in the following section.

1.5 Glacial Isostatic Adjustment

Glacial isostatic adjustment, or GIA, is the response of the Earth to the growth and retreat of glacial ice. GIA generates vertical and horizontal crustal motions and gravitational change. Observations of the effects of GIA are vital for constraining Earth rheology. Glacial mass changes influence the amount of water in the oceans, affecting global (eustatic) sea levels, while vertical land motions and gravitational changes driven by GIA also contribute to the differences in local sea levels relative to the eustatic sea level. Due to surface loading by the ice sheets, the lithosphere under the Cordilleran Ice Sheet was depressed up to 250 m isostatically (Shugar *et al*., 2014). Therefore, relative sea level (RSL) changes during the glaciation and deglaciation in the Coast Mountains/CSZ region were determined by relative magnitudes of vertical land displacement (isostatic depression) brought about by changing surface loads and the global warming eustatic sea-level changes. In contrast, far away from the ice sheets, RSL is governed largely by eustatic sea-level changes (Shugar *et al*., 2014).

During and following the deglaciation period, eustatic sea level rose while the land began to rise to pre-glaciation elevations. As the RSL curves in Figure 1.7 show, the isostatic uplift occurred relatively rapidly in the Coast Mountains/CSZ region when compared to the uplift around an area like Hudson Bay, part of the much older North American Craton. These different rates of the RSL change can help constrain important Earth rheological parameters, such as mantle viscosity. The rates of RSL change in Figure 1.7A

and 1.7B are very different, with the CSZ experiencing the majority of its change within 2 thousand years, while the Hudson Bay RSL change took almost 10 thousand years.

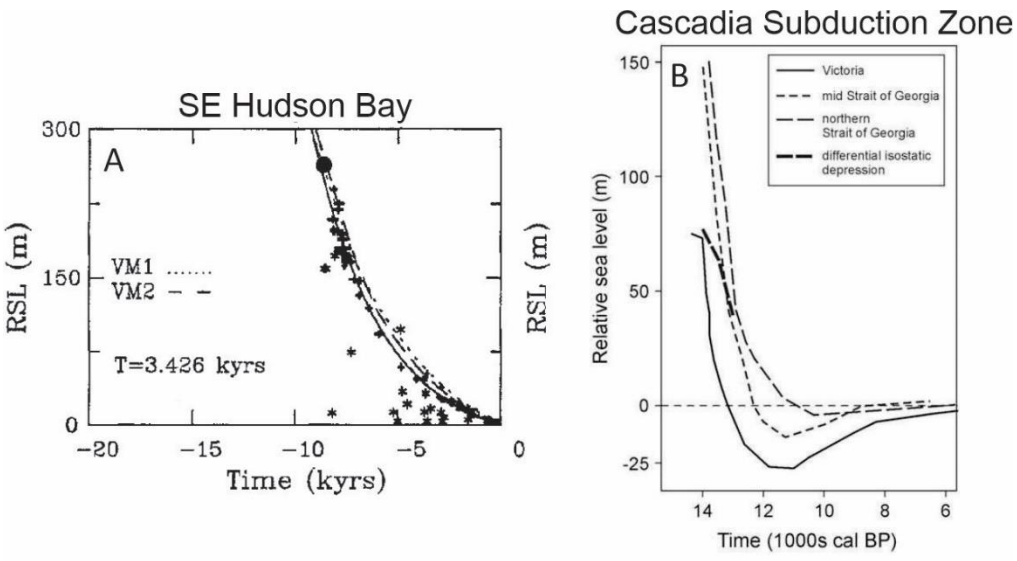

Figure 1.7: *(A) RSL data for SE Hudson Bay and predicted sea-level change for ICE-4G with the VM1 and VM2 viscosity profile models (Peltier, 2004) (B) Comparison of three RSL curves above the Cascadia Subduction Zone (see location map; Figure 1.8) From James et al. (2009a)*

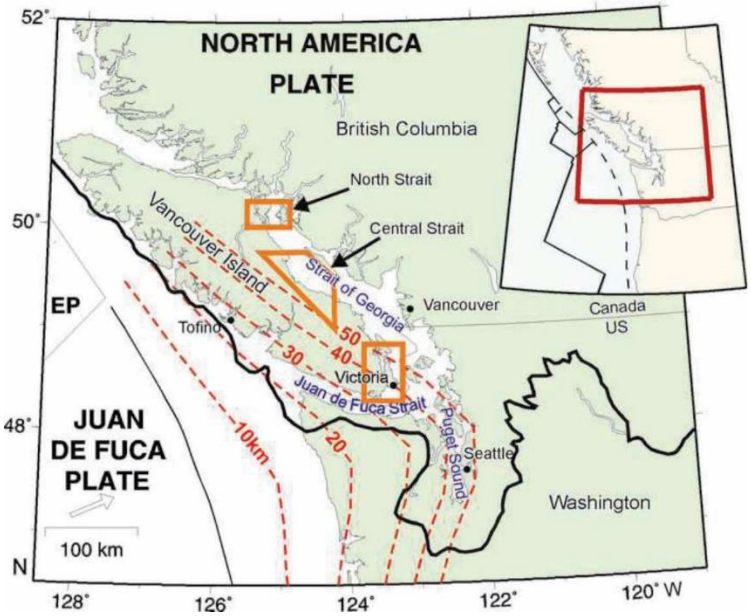

Figure 1.8: *Location map of the three RSL curves shown in Figure 1.7B. Original sources are northern Strait of Georgia (James et al., 2005), central Strait of Georgia (Hutchinson et al., 2004), and Victoria (James et al., 2009a). From James et al. (2009a).*

The significantly faster RSL change in the CSZ region suggests that shallow mantle viscosity in the CSZ is much smaller than in the Hudson Bay region. It is possible to estimate the different viscosities between

the two regions from the RSL curves and using the simple surface loading theory for postglacial rebound (GIA) from Turcotte and Schubert (2002):

$$D = D_0 e^{-\frac{t}{\tau}} \tag{1.1}$$

where D is the isostatic depression at a time t, D_0 is the initial isostatic depression after removal of the ice load, and τ is the exponential relaxation time (Turcotte and Schubert, 2002; James *et al*., 2005). τ is dependent on the mantle viscosity and is given by:

$$\tau = \frac{4\pi\mu}{\rho g \lambda} \tag{1.2}$$

where μ is viscosity, ρ is the density of the mantle (taken as 3300 kg m^{-3}), g is the universal gravitation constant (9.8 m s^{-2}), and λ is the wavelength of the load (Turcotte and Schubert, 2002). The relaxation time represents the time it takes the isostatic depression, D, to relax to e^{-1} of the initial displacement D_0.

Peltier (2004) provides a decay time of 3426 years in Figure 1.7A and taking the wavelength of 5000 km for the Laurentide Ice Sheet from Turcotte and Schubert (2002) it is possible to solve Equation 1.2 for μ, arriving at an approximate mantle viscosity of 1.4×10^{21} Pa s for Hudson Bay.

For the CSZ RSL curve in Figure 1.7B, an approximate τ of 850 years can be inferred from applying Equation 1.1 to the curve. The λ can be estimated to be 400 km, half the load or half the approximate width of the Cordilleran Ice Sheet. These values lead to a mantle viscosity estimate of 2.8×10^{19} Pa s, 2 orders of magnitude less than Hudson Bay.

While these values are rough estimates, the magnitude of the difference between the viscosities of the two regions is evidence of lateral heterogeneity in the global mantle viscosity. Further evidence of the

differences between the two areas in upper mantle viscosity as well as lithospheric thickness, can be seen from the analysis of heat flow of the two regions.

1.6 Heat Flow

Heat flow (or heat flux) is the flow of heat from the mantle to the Earth's surface. Areas of high heat flow are associated with a lower asthenosphere viscosity due to a hotter asthenosphere (Hyndman *et al.*, 2005). The Hudson Bay area sits atop some of the thickest lithosphere, with thicknesses ranging from 120 to 250 km around the bay's coast (Porritt *et al.*, 2015), with mantle heat flow measuring somewhere between 11 and 18 mW m^{-2} (Shapiro *et al*., 2004). The low heat flow lends to the high values for mantle viscosity that have been calculated from GIA measurements, on the order of 10^{21} Pa s (Mitrovica and Peltier, 1992). In contrast, the southwestern British Columbia region (containing the Coast Mountains and the CSZ) has a relatively thin lithosphere thanks to the active subduction of oceanic lithosphere at the CSZ (Cianetti *et al.,* 2002). Figure 1.9 is a map of the heat flow in the area, showing heat flow

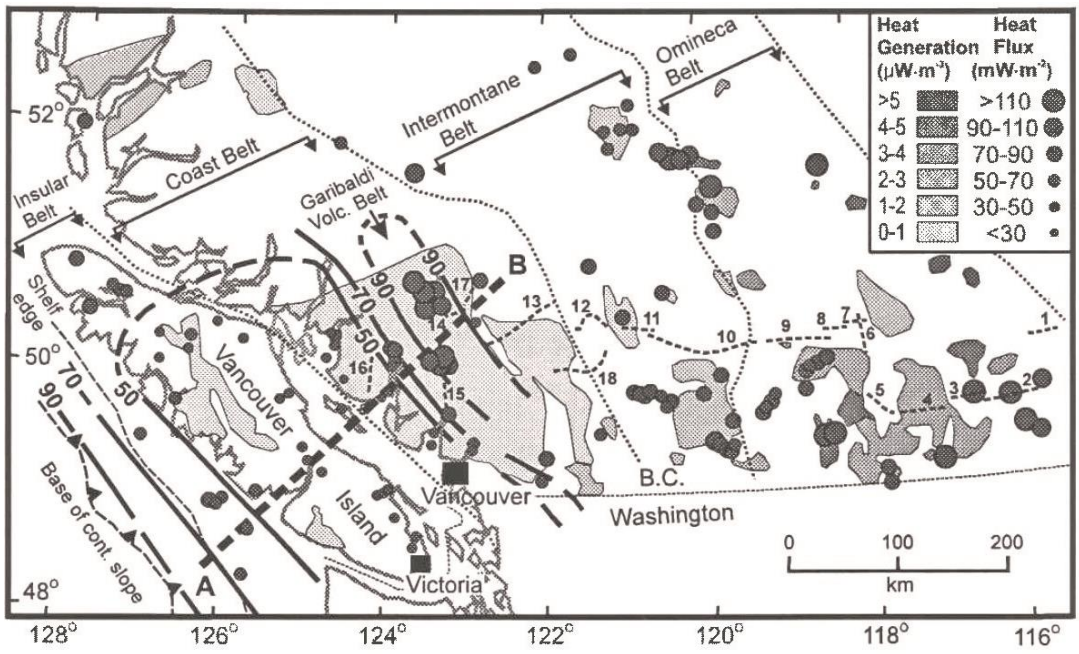

Figure 1.9*: Map of heat flow data in southwestern British Columbia. Heat flow contours (solid black lines parallel to margin) are highest at the deep-sea margin, lower over Vancouver Island, and become high again around the Garibaldi Volcanic Arc. Other features include the boundaries of main geological belts (dotted lines), and the Lithoprobe seismic reflection lines (thin, numbered, dashed lines) (Hyndman and Lewis, 1995).*

contours, with values ranging from less than 50 mW m^{-2} to as high as 90 mW m^{-2} around the volcanic arc (Hyndman and Lewis, 1995), much higher than the 11-18 mW m^{-2} values around Hudson Bay. Therefore, it is possible to infer a smaller value for viscosity in the Coast Mountains and CSZ region due to high heat flow. This conclusion is further backed up by reviewing the predicted Earth rheology from GIA models.

1.7 GIA Modelling

GIA models include an ice load model and an Earth model. The ice load model represents the magnitude and spatial distribution of the loading and unloading of glacial ice through time. The Earth model contains the rheological properties of the Earth that will respond to the ice load changes dictated by the ice load model.

GIA models constrain Earth model parameters such as effective lithospheric thickness, defined as the depth to the "brittle-ductile transition" (Currie and Hyndman, 2006), and mantle viscosity, through comparison with observations of actual GIA, such as RSL changes. Possible rheology values can be investigated by testing a range of values for each parameter and how they best fit to the observations. While this study focuses primarily on Global Navigation Satellite System (GNSS) vertical crustal motion data, past GIA modelling studies in the region have used RSL and shoreline tilts in order to constrain Earth rheology in the CSZ region (e.g., James *et al*., 2000, 2009b; Yousefi *et al*., 2018).

Global models have been developed in order to predict large scale GIA with the goal of averaging parameters to fit anywhere in the world. The ICE-4G global model, informed by the Hudson Bay viscosity, provides good fit with the RSL curves in Figure 1.7A with upper mantle viscosity of 10^{21} Pa s (Peltier, 2004). The updated global ICE-6G and ICE-7G models employ viscosity profiles with an average upper mantle viscosity of 4.5×10^{20} Pa s (Peltier et al., 2013; Roy and Peltier, 2018). Both values are up to 2 orders of magnitude larger than those found from modeling GIA around the CSZ, in the range of 10^{18}

to 10^{19} Pa s. Researchers have developed several models that are specific to the area of interest of this study, discussed in detail below.

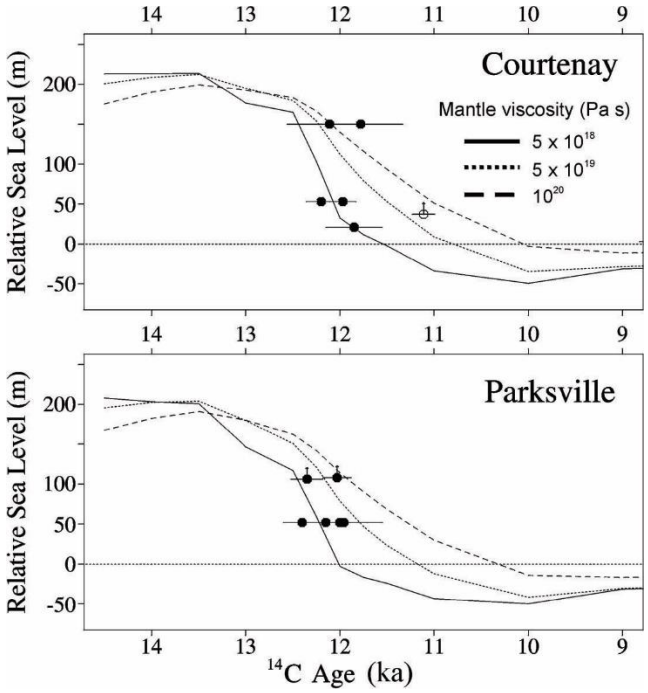

Figure 1.10: *Modeled RSL curves for three uniform mantle viscosities and a fixed lithospheric thickness of 35 km, compared to the RSL observations for both Courtenay and Parksville (James et al., 2000). A Courtenay data point that is inconsistent with the others is shown as an open circle.*

As shown in section 1.6, differences in viscosity can be approximated with an estimate of decay times and load wavelengths. The varying isostatic responses to different values for upper mantle viscosity can be more robustly represented through modelling. For example, Figure 1.10 shows model predictions of RSL in two locations around Vancouver Island for three mantle viscosity values (James *et al*., 2000). Figure 1.10 shows that by changing the mantle viscosity causes the isostatic response to noticeably change. James *et al.* (2000) used shoreline tilts of two proglacial lakes, Lake Russell Hood and Lake Bretz, in Puget Sound, to provide constraints on shallow mantle viscosity in the CSZ (James *et al*., 2000). Combinations of upper mantle viscosity and lithospheric thickness were found that fit the shoreline tilt observations for each lake, and considering both lakes, it was possible to find a common solution. A mantle viscosity of 5×10^{18} Pa s and a lithospheric thickness of about 35 km were found to best fit the shoreline tilt data with this ice load model (James *et al*., 2000). Figure 1.11 shows results of a sensitivity

analysis from James *et al.* (2000) where various scenarios were tested on the GIA model such as a smaller ice sheet, larger ice sheet, late deglaciation, and possible slip on the Seattle fault. Regardless of scenario the mantle viscosity was found to always be less than about 10^{20} Pa s.

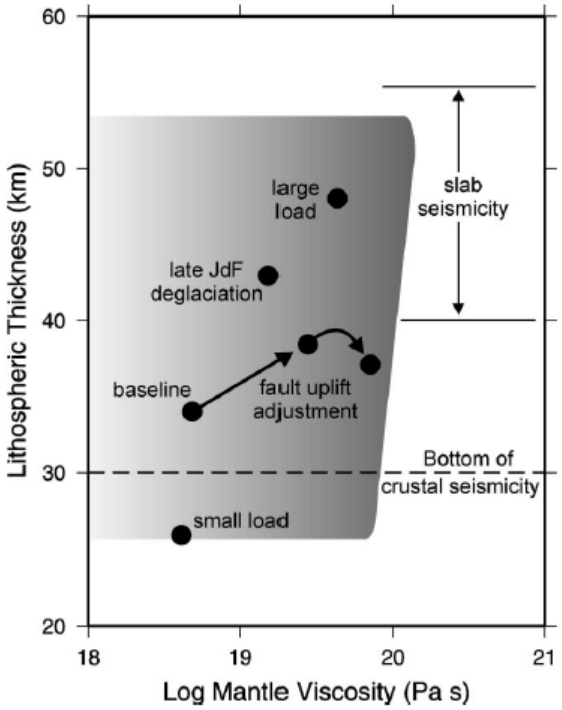

Figure 1.11: *Results from James et al. (2000) sensitivity analysis. Filled circles represent the baseline solution, effects of possible slip on the Seattle fault, larger ice load, a smaller ice load, and a later Juan de Fuca strait deglaciation (delayed 1500 yrs). The shaded area represents the possible range of solutions for these effects.*

Clague and James (2002) used a more complex, 5-layer Earth model where the mantle is broken up into three layers of its own:

1. The asthenosphere: from the base of the lithosphere to a depth of 440 km
2. The Transition Zone: from 440 to 670 km deep
3. The Lower Mantle: 670 km to the core-mantle boundary

The authors used the same RSL data and three modeled mantle viscosities as in James *et al.* (2000), with differing scenarios based on lithospheric thickness and ice load size. As shown in Figure 1.12A and 1.12B, the RSL predictions for 60 km thick lithosphere follow a similar pattern as the 35 km predictions (Figure 1.10) but underestimate the magnitude of the isostatic response. The increased flexural rigidity of the

thicker lithosphere reduces subsidence by supporting more of the ice load (James *et al*., 2002). With the 60 km thick lithosphere it is still possible to obtain a good fit with the RSL observations by increasing the load to 1.2 times its original magnitude, as shown in Figure 1.12C and 1.12D. The authors concluded that the mantle viscosity is less than 10^{20} Pa s, with 5×10^{18} Pa s being the preferred value (Clague and James, 2002).

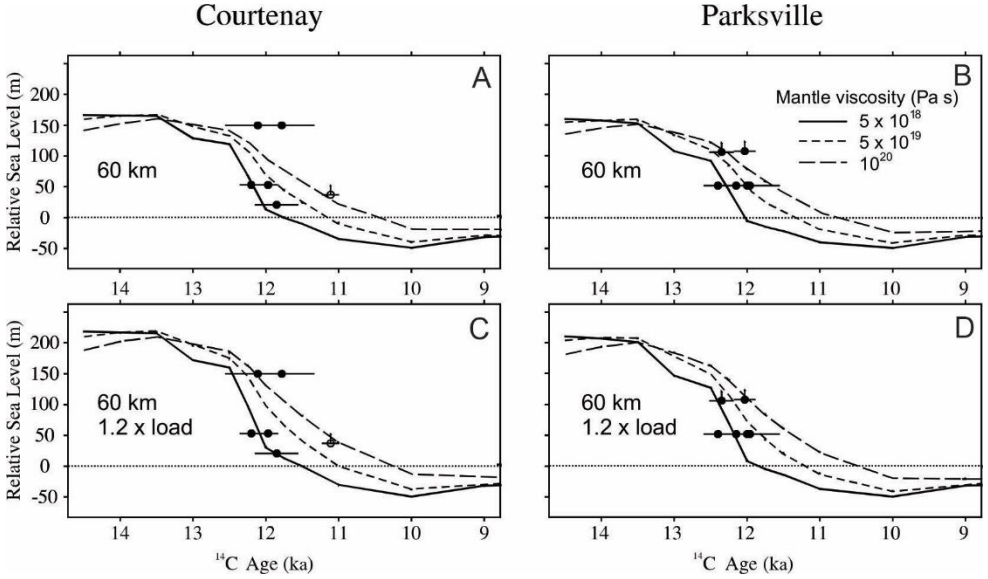

Figure 1.12: *Modeled RSL for the same three uniform mantle viscosities as Figure 1.10 compared to RSL observations at Courtenay and Parksville. A) and B) have fixed lithospheric thicknesses of 60 km and use the base ice load for the modeled Cordilleran Ice Sheet. C) and D) have the same 60 km lithosphere but with an ice load scaled up by a factor of 1.2. A Courtenay data point that is inconsistent with the others is shown as an open circle. Adapted from James and Clague (2002).*

James *et al.* (2009b) used the RSL curves from Figure 1.7B to constrain earth rheological parameters near the CSZ. These RSL curves are from three locations around Vancouver Island (Figure 1.8): northern Strait of Georgia (James *et al*., 2005), central Strait of Georgia (Hutchinson *et al*., 2004), and Victoria (James *et al*., 2009a). Assuming a 60 km thick lithosphere in order to account for the depth to the top of the subducting slab, James *et al.* (2009b) found that there was a clear relationship between asthenospheric thickness and which viscosity best fit the RSL curves. Figure 1.13 shows the model results compared to the RSL curves. Each plot in Figure 1.13 represents an Earth model with different asthenospheric thickness, along with the viscosity that led to the best fit for each of the different

thicknesses. The resulting best fitting viscosities ranged from 3×10^{18} Pa s to 4×10^{19} Pa s with asthenospheric thicknesses from 140 km to 380 km (James *et al*., 2009b).

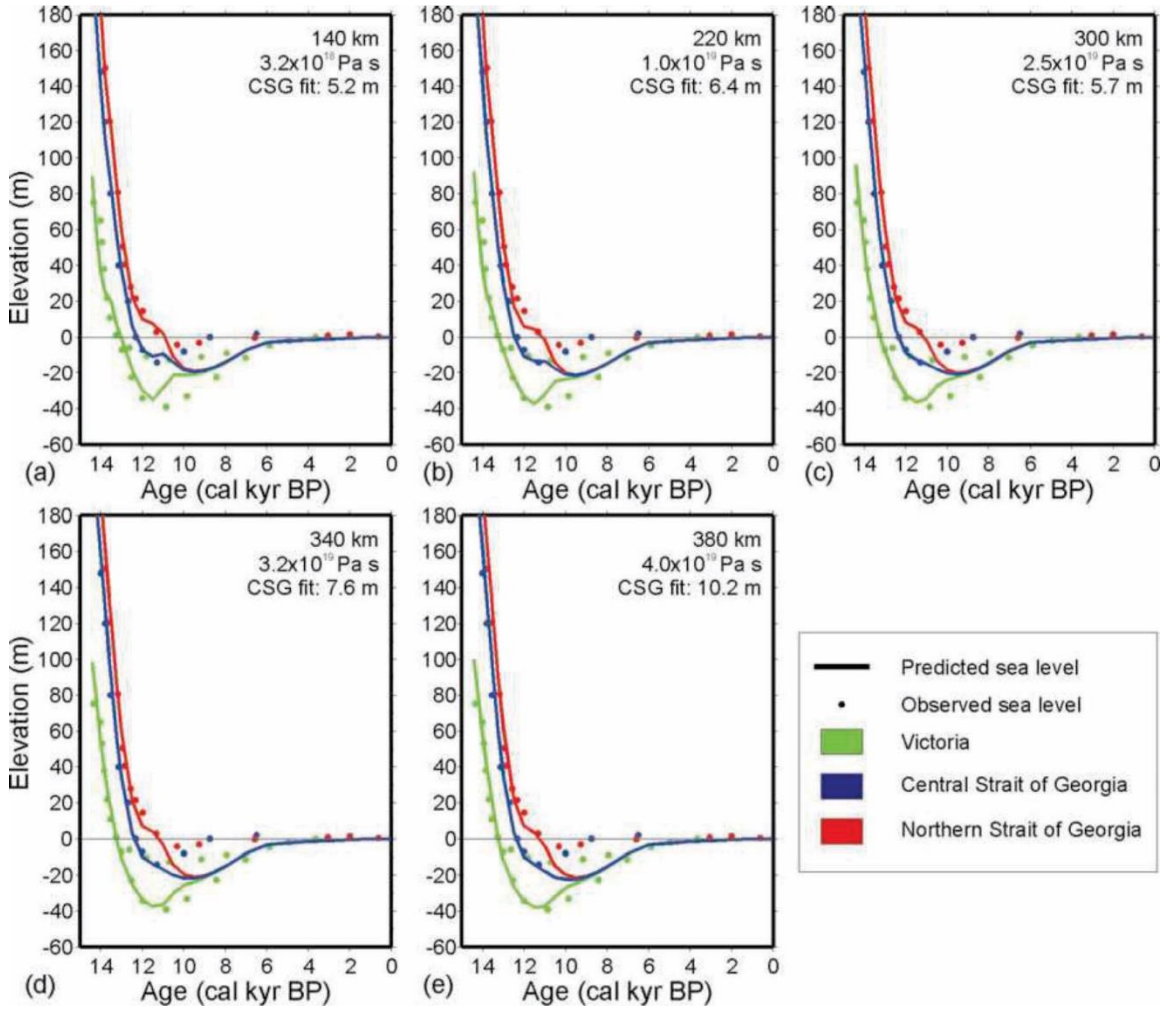

Figure 1.13*: Comparison of predicted sea level (shown as the solid lines) and observed sea level (shown as points) for the three locations around Vancouver Island. The RMS fit of the Central Strait of Georgia (CSG) sea level curve and the best fitting viscosity are given for each modeled asthenospheric thickness (shown top right of each plot) (James et al. 2009b).*

A more recent study focused on the west coast of North America, with a separate section that includes the Southern Coast Mountains and Vancouver Island, again used RSL data for the Fraser glaciation period to constrain GIA model parameters (Yousefi *et al*., 2018). The model tested a range of lithospheric thicknesses as well as upper mantle viscosities. The minimum data-model misfit results show a lithospheric thickness of 46 km and an upper mantle viscosity of 5×10^{19} Pa s. This is in good agreement with the previous studies mentioned earlier. After applying data weighting to improve

accuracy, the best fit for the upper mantle viscosity decreased by an order of magnitude to 5×10^{18} Pa s. However, the authors note that they were unable to produce satisfactory fits to both sets of RSL data for this region. It is noted that this could be due to the influence of long-term tectonic effects that are not well quantified or a shortcoming in the Earth component of the model, such as not incorporating lateral variability and not accounting for nonlinear deformation.

In summary, previous work in the Coast Mountains' area and the CSZ have found that global GIA model parameters, that fit well with the Hudson Bay region, cannot be applied to these regions. In contrast to the asthenospheric viscosities on the order of 10^{21} and 10^{20} Pa s derived from the Hudson Bay region, similar studies in the CSZ have derived viscosities on the order of 10^{18} and 10^{19} Pa s.

1.8 Summary

The tectonic history and present tectonic activity of the Coast Mountains is reflected in high heat flow, indicative of a relatively thin lithosphere and low asthenospheric/upper mantle viscosity. Previous GIA modelling undertaken in the region provides some quantitative constraints on the low asthenospheric viscosity and thin lithosphere, compared to the stable cratonic region surrounding Hudson Bay. The region has an extensive and complex glacial history that remains active to this day. While most of the effects of the last glacial maximum rapidly dissipated due to low asthenospheric viscosity, the region is sensitive to glacial change, such as the rapid decay of Little Ice Age glaciers. The rest of this study will discuss an approach to quantifying the effects of the Little Ice Age glacier change and how this can further constrain GIA model parameters and increase our understanding of Earth structure in this region.

This thesis contains five sections, including this background chapter. Chapter 2 introduces the GNSS observational data used to tune the GIA models. Chapter 3 describes the methodology of the study, including the ice load history models, earth models, and statistical method for model result comparison

to GNSS observables. Chapter 4 shows the results of the GIA models for the Coast Mountains region constrained by the GNSS observables from Chapter 2, as well as an adjusted set of GNSS uplifts to account for other possible sources of vertical land motion. Additionally, Chapter 4 contains a discussion of how the results compare to past GIA models and how the current model can be improved. Finally, Chapter 5 contains a summary of all the previous chapters and concludes this study.

Chapter 2: Observations

2.1 Introduction

Glacial Isostatic Adjustment (GIA) models are tuned by comparing model predictions to observations of vertical land motion, relative sea-level change, and other geodetic observables. Vertical motion data come in different forms, including relative sea-level histories from coastal deposits, tide gauge trends, multi-epoch geodetic leveling, and continuous and episodic Global Navigation Satellite System (GNSS) observations. GNSS refers to the various systems of satellites providing positioning and timing data to receivers. GNSS is an umbrella term that includes all global satellite positioning systems. This study focuses on vertical land motion (VLM) measured by the Global Positioning System (GPS), which is one of the GNSS systems in operation.

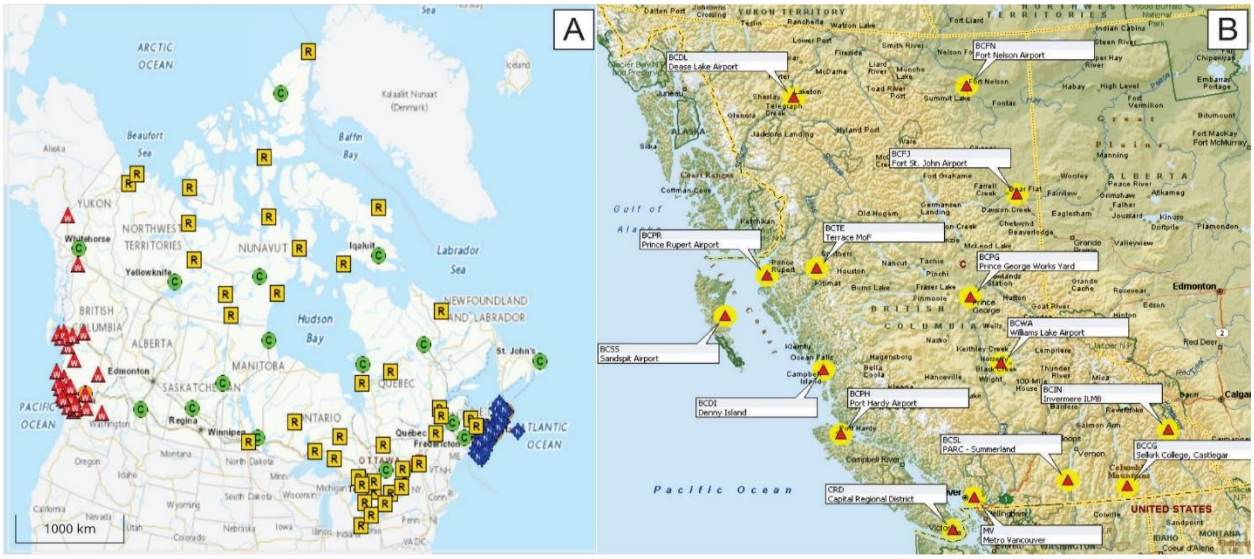

Figure 2.1*: A) The Canadian Active Control System map (CACS), with the Western Canada Deformation Array (WCDA) as red triangles (NRCan, 2018). B) the British Columbia Active Control System (BCACS) GNSS station map (Province of British Columbia, 2016).*

The GNSS data used in this study are provided by the Western Canada Deformation Array (WCDA) and British Columbia Active Control System (BCACS) GNSS stations. The WCDA is part of the Canadian Active Control System (CACS), a network of continuously-tracking GNSS multi-frequency receivers across

Canada; the stations are known as Active Control Points (ACPs). A map of the CACS (Figure 2.1a) shows the distribution of ACPs across the country, including the WCDA as red triangles (NRCan, 2018). The BCACS contains 20 continuously tracking permanent GNSS station receivers strategically located around the province (Figure 2.1b) (B.C. Active Control System (BCACS) - Province of British Columbia, 2021).

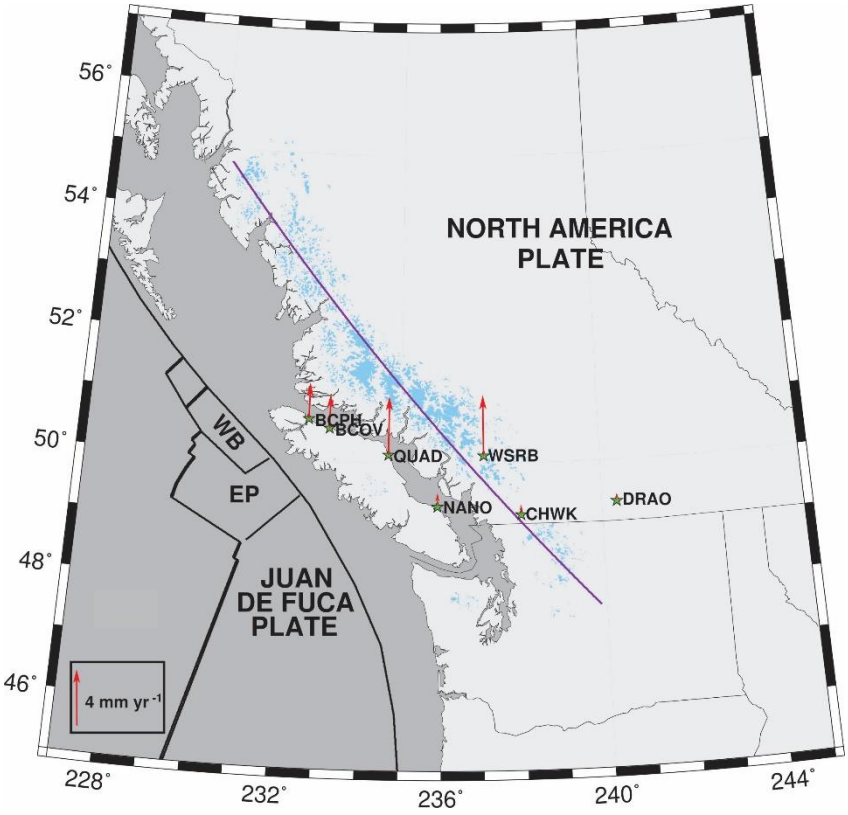

Figure 2.2: *Selected GNSS sites from BCACS and WCDA. Red arrows indicate the VLM measured at the site (velocities given in Table 2.1). Sites more than 200 km from Coast Mountain Range axis (purple line) were not employed in the analysis. Current ice extent is in blue.*

The distribution of GNSS sites in both the BCACS and WCDA within the Coast Mountains region does not provide an extensive observational dataset to robustly document deformation and land motion. This study uses a selection of GNSS stations, from the two sources, that operated a sufficiently long time (in this study, more than 5 years) so that a linear vertical signal can be derived. Seven WCDA and BCACS stations were selected, prioritizing locations in the SCM region based on the following criteria: proximity to the mountain range axis (Figure 2.2), probable absence of a substantial interseismic or postseismic

signal in their measured uplift, and antenna monuments located on bedrock. Sites located more than about 200 km from the mountains were excluded to focus on the expected signal from Coast Mountain glacier fluctuations. Sites in the north coastal part of the study area, Bella Coola and further north, have been shown to have continued post-seismic deformation as part of their uplift signals, due to the 2012 Haida Gwaii earthquake (Nykolaishen et al., 2015; Jiang et al., 2021a) and were excluded. Stations on the west coast of Vancouver Island are also excluded as they are close enough to the tectonic margin to be potentially affected by interseismic deformation. Finally, out of the stations in the Vancouver area and along the southern border with the United States, Chilliwack (CHWK) and the Dominion Radio Astrophysical Observatory (DRAO) located near Penticton were chosen for their long time series and location. Table 2.1 and Figure 2.2 show the final selected GNSS stations.

2.2 Contributions from Other Processes

Three potentially important sources of uplift from processes other than Little Ice Age GIA are VLM from terrestrial water changes, interseismic deformation from the active subduction zone, and residual GIA from the retreat of the Cordilleran Ice Sheet. Figure 2.3 shows VLM predictions from a groundwater model and an interseismic deformation model (Yousefi *et al*., 2020). The ground water contribution model used a 0.5° X 0.5° spatially variable annual groundwater distribution for the years 1900 to 2011 (Wada *et al.,* 2012). The annual groundwater distribution is based on a global hydrological model that takes the difference between groundwater recharge and human-induced extraction. It found negligible values of uplift in the Coast Mountain study area. Yousefi *et al.* (2020) used the interseismic model developed by Li *et al.* (2018) to predict -1 to -2 mm yr^{-1} VLM in the SCM area using a lithospheric thickness of 46 km and upper mantle viscosity of 5×10^{19} Pa s (Li *et al.,* 2018). Krogstad *et al.* (2016) analyzed east-west levelling campaigns in several locations on the Pacific Coast of the United States. The levelling campaign near Neah Bay, which runs east towards Seattle, is close to this study's region of interest but lies on the periphery, outside of predicted GIA uplift. In partial contradiction to the results

of the Li *et al.* (2018) model, this levelling campaign found that interseismic VLM approaches 0 as the campaign goes east, measuring 0 mm yr^{-1} for several benchmarks in the region just north of Seattle, where the Li *et al.* (2018) model predicted subsidence. Due to the uncertainty of whether there is interseismic VLM in the area, the GNSS observations are not corrected for interseismic deformation in our initial analysis in Chapter 4. We also examine the consequences of correcting the GNSS data with Li *et al.'s* (2018) interseismic deformation rates.

A third possible source of vertical land motion is residual GIA from the retreat of the Cordilleran Ice Sheet. This effect is thought to be small and may be approximated by averaging vertical land motion from interior sites located away from the Coast Mountains. In Chapter 4 we carry out an initial analysis that does not include this effect, and then we examine the consequences of applying a correction for this possible additional source of vertical land motion.

Table 2.1: 7 GNSS sites and their coordinate locations, observed uplift rate and calculated error[1]

Station Name	Latitude	Longitude	Uplift (mm yr^{-1})	Error (mm yr^{-1})
BCPH	50° 41' 8.028"	-127° 22' 31.270"	2.53	0.12
BCOV	50° 32' 39.412"	-126° 50' 33.513"	2.38	0.12
QUAD	50° 7' 56.981"	-125° 19' 50.991"	4.11	0.13
WSRB	50° 7' 35.541"	- 122° 55' 16.284"	4.29	0.10
NANO	49° 17' 41.318"	-124° 5' 11.325"	1.01	0.05
CHWK	49° 9' 23.760"	-122° 0' 28.800"	0.72	0.07
DRAO	49° 19' 21.360"	- 119° 37' 300"	0.49	0.05

[1] Error is calculated as a combination of white (not time dependent) and coloured (time-correlated)

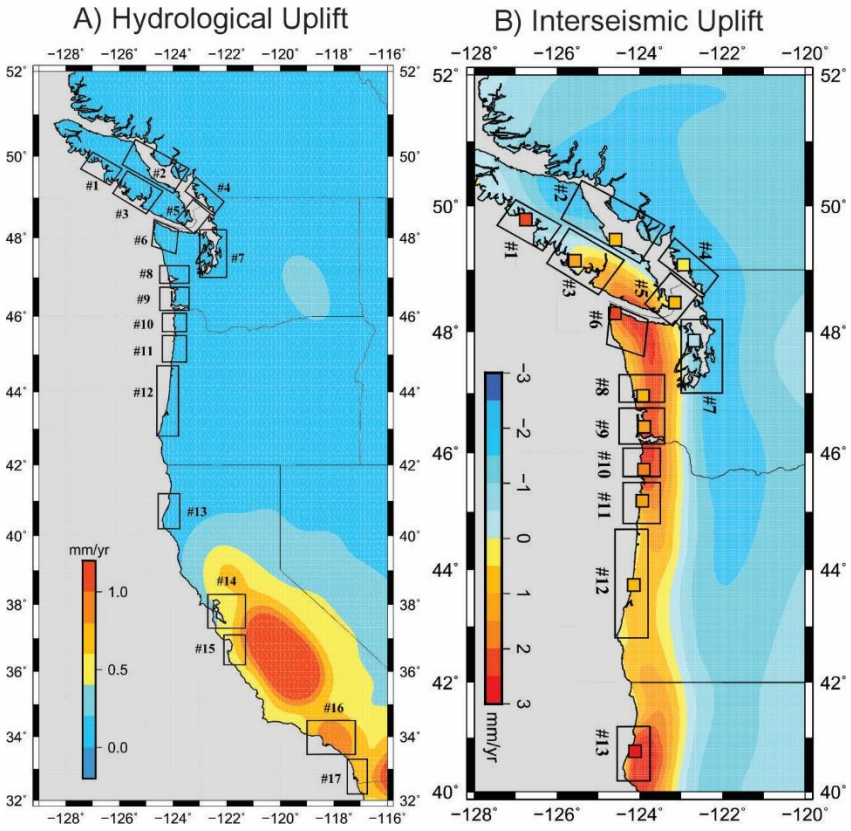

***Figure 2.3**: A) hydrological groundwater induced uplift rates, B) Interseismic deformation model VLM predictions for a lithospheric thickness of 46 km and upper mantle viscosity of 5×10^{19} Pa s, square symbols represent the observed vertical land velocity at those points. The interseismic deformation model used a limiting locking depth of 80 km, smoothness factor of 400, and maximum back slip rate of 40 mm yr^{-1} (Yousefi et al., 2020). Figure adapted from Yousefi et al. (2020).*

2.3 GNSS Station Time-Series Analysis

The GPS data were analyzed using GIPSY 6.4 software from the Jet Propulsion Lab (JPL) (Jiang *et al.*, 2021), following the Precise Point Positioning (PPP) processing strategy outlined by Jiang *et al.* (2012). PPP is a positioning technique that solves for an accurate antenna position using a single GNSS receiver. It relies on precise GNSS satellite clock corrections and positions, typically calculated from a global reference station network which allow for analysis of single receiver data using receiver-specific parameters (Zumberge *et al*., 1997). The PPP analysis in this study used satellite position and clock files provided by the Jet Propulsion Laboratory (JPL) in the ITRF 2014 global reference frame (Jiang *et al*., 2021).

A time series analysis of the processed data was carried out for each station, in which a linear trend, seasonal and annual sinusoidal terms, and offsets from station maintenance are simultaneously solved using least-squares techniques. The uncertainty in the uplift rate is derived by scaling the formal error by an estimate of the coloured noise. Unlike white noise, which can be significantly reduced by averaging frequent measurements, coloured noise is time-correlated and not easily reduced from continued data collection (Mao *et al*., 1999).

2.4 Chosen GNSS Observational Data

Table 2.1 shows the processed uplift rates and uncertainties of each selected site. Figure 2.4 shows the vertical velocity time-series for each of the 7 sites. Offsets arise from antenna and receiver changes and other maintenance carried out at sites and are shown as the green dotted lines. The annual and sub-annual oscillations in the GNSS signals come from a variety of possible sources including atmospheric loading, hydrological loading, thermal expansion of the instruments, variations in tropospheric delay (Klos *et al.,* 2018), and seasonal ice mass changes driving elastic earth responses from the changes in ice loading (Bevis *et al.,* 2012). Utilizing this method, changes in the antenna models, antenna heights, and repairs are accounted for in the continuous time-series.

The uplift rates of the seven sites range from 0.49 mm yr^{-1} (DRAO) to 4.25 mm yr^{-1} (WSRB). The largest vertical velocities come from WSRB and QUAD (4.11 mm yr^{-1}) which are the two sites closest to large ice masses. WSRB is the amalgamated WSLR (up to the end of 2016) and WSLB (2016 and onward) GPS site located near Whistler BC, within the Coast Mountains and is the site nearest to regions of major ice mass loss. QUAD is located on Quadra Island between the mainland BC Coast Mountains and Vancouver Island.

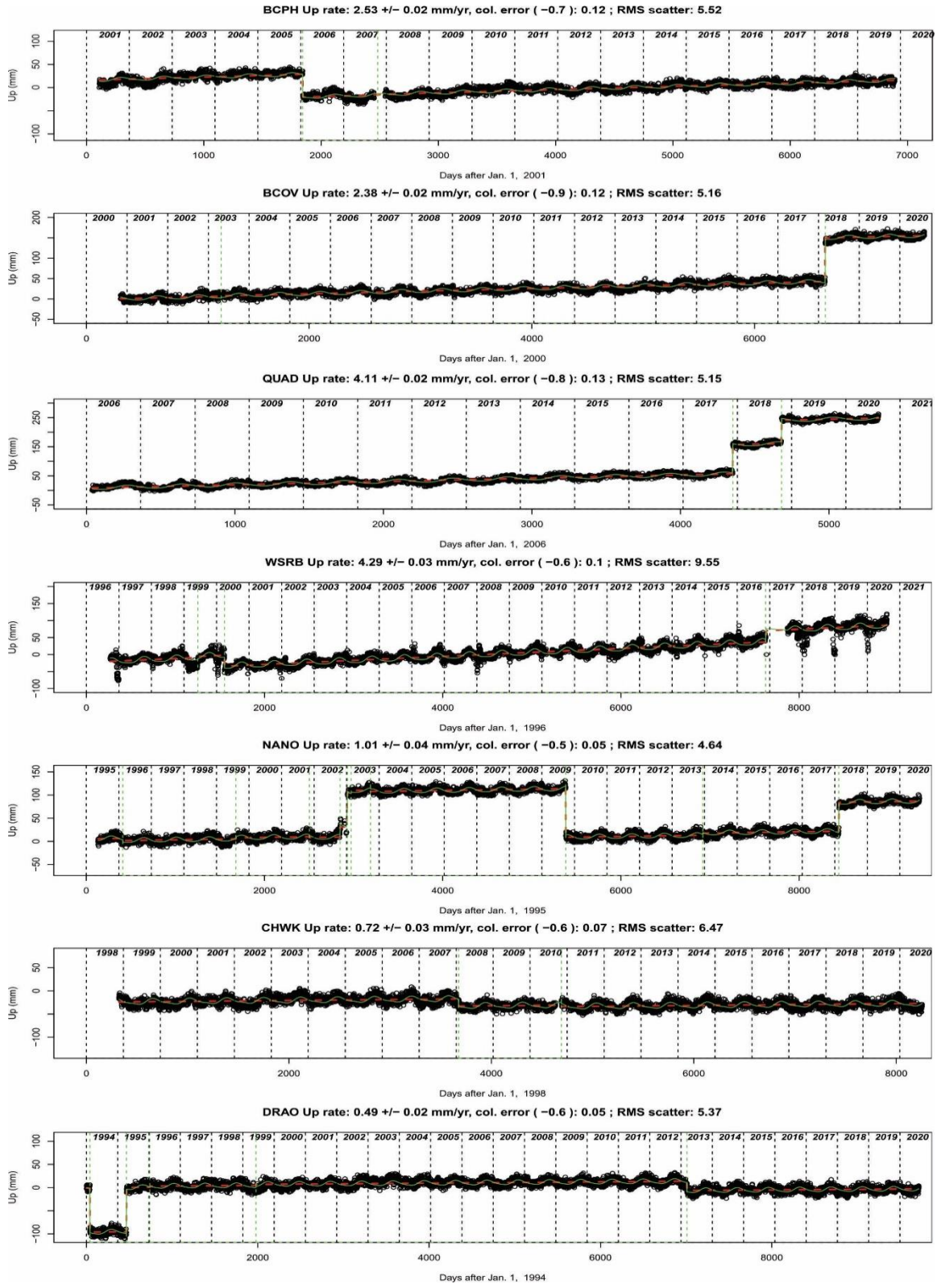

Figure 2.4*: Vertical velocity time-series for each of the 7 sites, plotted from the earliest available data to the latest (varies between sites). WSRB is the amalgamated WSLR (up to the end of 2016) and WSLB (2016 and onward) at the same location. Green dashed lines indicate applied offsets to the time-series.*

Chapter 3: Methods

3.1 Overview

A GIA model is composed of an ice loading history and an earth model, and both components are required to generate predictions of vertical land motion (VLM). The ice loading history is a model of ice growth and decay used to simulate the changes in the overall surface load over a specified period of time. In this study, two different approaches are taken for the ice loading history. Ice Load A features a simple uniform thickness change over three time-steps, while Ice Load B incorporates a more complex 17 time-step history. For Ice Load B, a number of load variants are generated corresponding to different volume-area scalings (Bahr *et al*., 1997).

The Preliminary Reference Earth Model (PREM; Dziewonski and Anderson, 1981) specifies the density and elastic parameter structure. The viscosity profile follows the VM5a viscosity structure (Peltier *et al*., 2015) for the transition zone and lower mantle. We examine a range of asthenospheric viscosities and effective elastic lithospheric thicknesses (referred to in the following simply as lithospheric thicknesses). The GIA model predictions are compared to the GNSS uplift rates from Chapter 2 and assessed with a goodness of fit test to find the best combinations of ice load history and rheological parameters.

3.2 Ice Loading Models

The ice load histories simulate the change in the surface loading from glacial ice as the glaciers fluctuate over time. The ice loads are provided on a 20 km x 20 km grid over the study area (Figure 1.1), where each grid cell contains a cylinder of ice with a fixed radius giving an area equivalent to the area of the grid cell. Changes in the height of these cylinders between different time-steps represent the histories of ice thickness fluctuations.

Two different ice load histories were developed using different approaches for the temporal fluctuations of glaciers and ice fields of the Coast Mountains. Both ice loads are based on gridded estimates of

present-day ice thicknesses for all glaciers in the region (Farinotti *et al*., 2019). These ice thicknesses are provided as GeoTIFF files in the supplement to Farinotti *et al*. (2019) and result from an ensemble model applied to the Randolph Glacier Inventory (RGI) version 6 outlines (RGI Consortium, 2017). The Coast Mountain RGI glacier outlines are referenced to dates between 2004 and 2006. For this study, for simplicity we assume that the thicknesses provided by Farinotti *et al*. apply to the year 2004. As the ice thicknesses provided are in very fine spatial resolution, ranging from 25 m to 100 m, they were averaged over each 20 km grid cell (Figure 3.1). The area was split into four subregions: Central Coast Mountain glaciers, Southern Coast Mountain glaciers, Insular Mountain Glaciers, and Washington Glaciers.

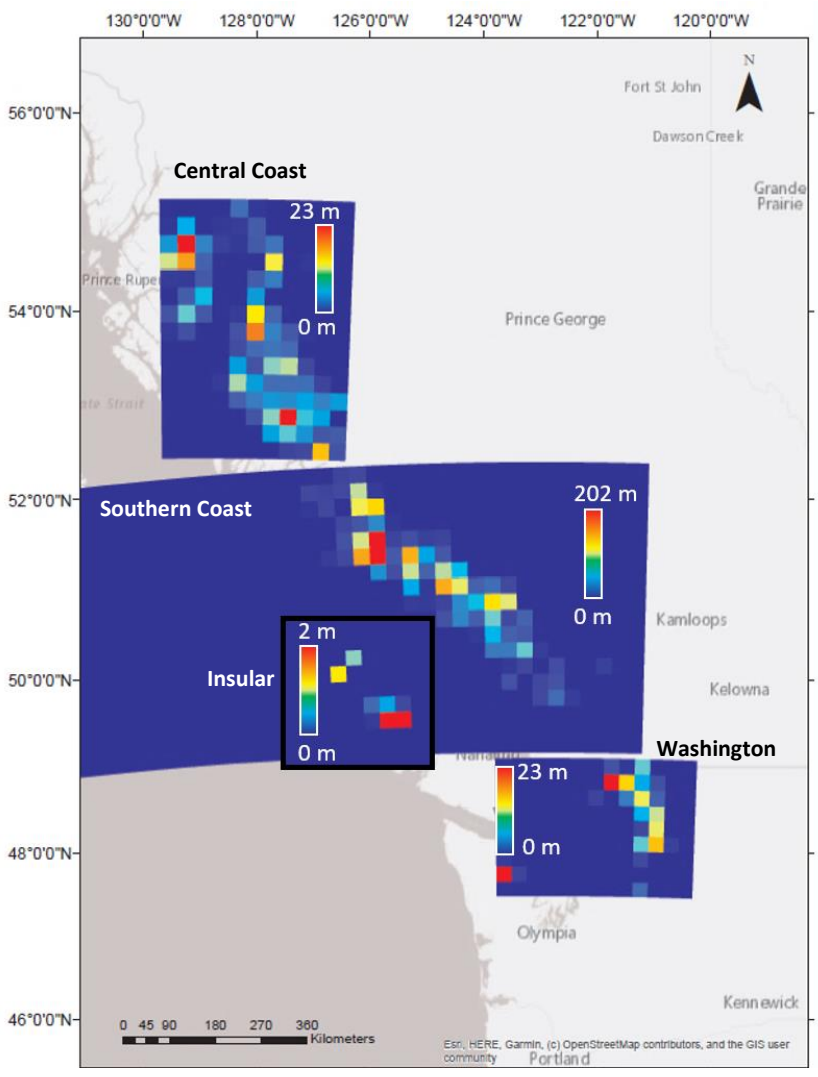

Figure 3.1*: Gridded present-day ice thicknesses (20 km by 20 km spatial resolution). Note the different scale bar for each of the four subregions.*

Ice load A uses a simple glacier volume versus time profile, linearly extrapolating modern ice melt rates back to the LIA maximum time, assumed to be around 1700 CE. This ice load is assumed to have a volume equivalent to the present-day volume around 1000 CE and grow linearly to the LIA maximum at 1700 CE. Ice load B utilizes a published profile of glacier change through time to better represent the timings and magnitudes of glacier volume change (Koch *et al*., 2009). The LIA maximum volumes were determined by applying a range of volume-area scaling coefficients to LIA areas for the Garibaldi Park glaciers (Koch *et al*., 2009), explained in more detail in section 3.2.2.

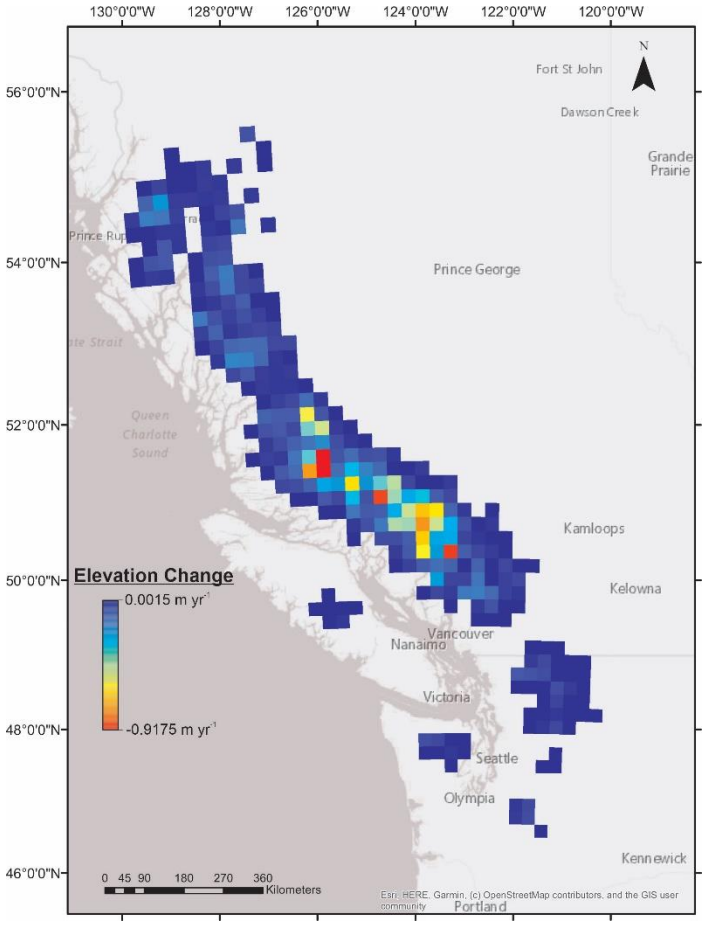

Figure 3.2*: Gridded average elevation change of ice (interpreted as melt rate for the ice load history model) from 2000-2019, based on ASTER data and for 20 km by 20 km regions. Data from Menounos et al. (2019).*

3.2.1 Ice Load A

Advanced Spaceborne Thermal Emission and Reflection Radiometer (ASTER) surveys were conducted for this region, leading to surface elevation change data for ice during the survey period of 2000 to 2019

(Menounos *et al*., 2019). The melt rate data from 2000-2018 were clipped to the RGI outlines, with any missing data points within the RGI areas set to 0 m yr^{-1}. The clipped melt data were then averaged over the same 20 km x 20 km grid as Figure 3.1 (Figure 3.2). The result was a corresponding melt rate for each grid cell.

Each grid point thickness was determined using each cell's melt rate. In this ice load history (ice load A), there are 3 time-steps. The first time is 1000 years before the present, where the ice thickness is assumed to be the same as the RGI value at 2004. The second time is the LIA maximum approximated by extrapolating the melt rate of each grid cell back to 300 years before the present. The third is the present time, assumed to be the thicknesses given in the RGI at 2004. Present day is taken as time 0 and the melt rates are extrapolated back 300 years from this point. The volume over time for Ice Load A is presented in Figure 3.3.

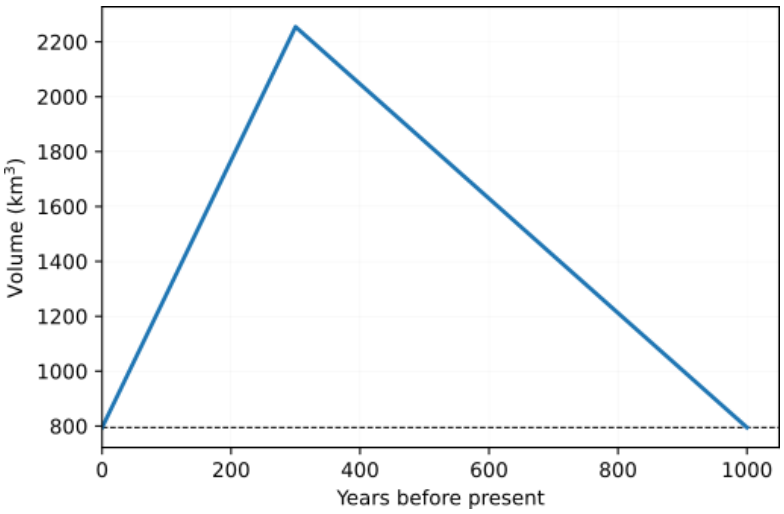

Figure 3.3: *Volume over time profile for Ice Load A (blue line). The black dashed line represents the volume used as the present-day volume (equivalent to the volume in 2004.*

3.2.2 Ice Load B

To generate Ice load B, the glacier volume-area scaling relationship (Bahr *et al*., 1997) was applied to modeled LIA maximum areas to find the percent increase from the RGI date. The Garibaldi normalized glacier extent profile from Koch *et al*. (2007) was digitized and used as a qualitative template for matching the scaled ice change with the times of maximum ice volume to create a more temporally accurate ice change history for each pixel. The qualitative glacier extent (Koch et al., 2007b) was assumed to be analogous to glacier area and needed to be scaled to represent changes in glacier volume using the volume-area relationship (Figure 3.4).

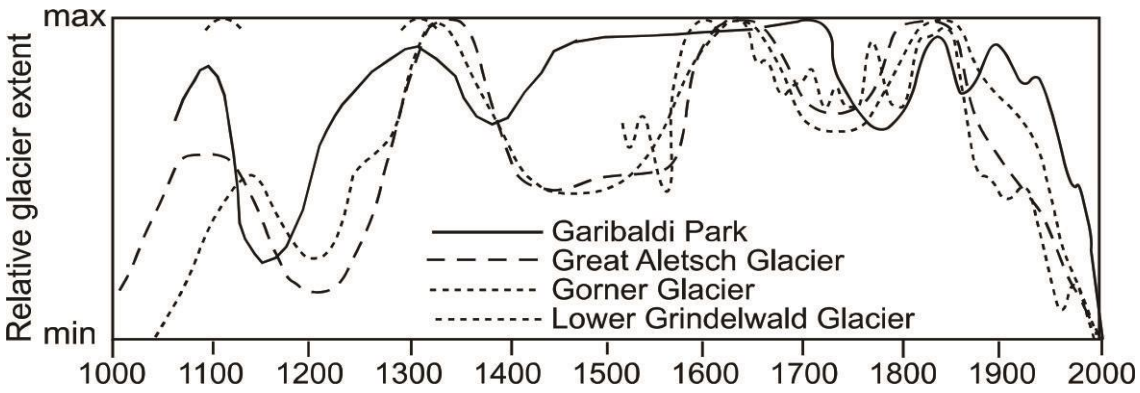

Figure 3.4*: Garibaldi extent history (solid line, Koch et al., 2007) is the profile used for the ice load models. The other profiles (dashed lines) refer to various European glaciers as a comparison*

The relationship between glacier volume and area, at glacial equilibrium, can be estimated using a power-law function:

$$V = cS^{\gamma} \tag{3.1}$$

where V is glacier volume, S is the glacier area, and c and γ are constants (Bahr *et al*., 1997). This volume-area scaling has been shown to fit empirical data and is derived using scaling analysis. To determine a starting point for the coefficients c and γ, the relationship between glacier volume and area was determined through an empirical fit to Equation 3.1. Starting with the gridded thickness distributions from Farinotti *et al*. (2019), present volume can be estimated. The available thickness

GeoTIFFs represent gridded ice thickness with the pixel value as ice thickness in metres and the pixel's representative size varying between images (between 25 and 100 metres).

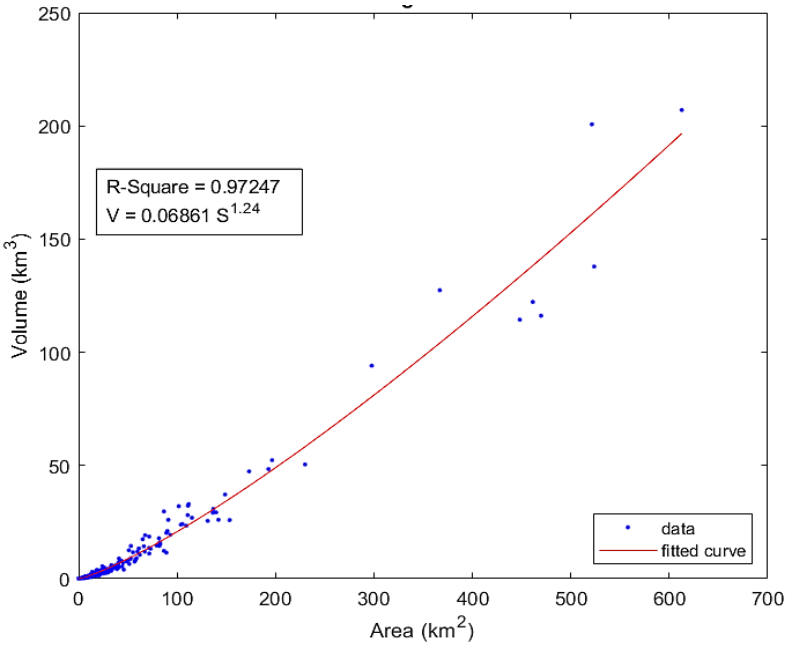

***Figure 3.5**: Plot of Volume vs Area for all glaciers in the region with the power law relationship fitted to the data. The derived coefficients are $c = 0.06861\ km^{3-2\gamma}$ and γ= 1.24 with an R^2 of around 0.973.*

The images corresponding to the Coast Mountain glaciers were resampled to all be the same resolution (in this case, 100 m x 100 m per pixel). Second, the pixel values were multiplied by the pixel area and then summed to find the estimated volume of each glacier. The area versus volume was plotted for all glaciers in the region, and Equation 3.1 was fitted to the data to determine c and γ (Figure 3.5). With an R-square fit of ~0.97, the region's derived coefficients are $c = 0.06861$ and γ= 1.24.

The values for c can vary widely between glaciers and its units ($km^{3-2\gamma}$) are dependent on γ. Values for c also vary within the literature but typically lie between ~0.0271 (Adhikari and Marshall, 2012; DeBeer and Sharp, 2007) and ~0.033 (Bahr *et al*., 1997, 2015). The exponent, γ, varies depending on glacier geometry and whether the glaciers are in a steady-state. Global values of 1.36 for valley glaciers and 1.22 for ice caps are typically accepted (Bahr *et al*., 1997, 2015). The γ value of 1.24 derived for the Coast Mountain glaciers is low as it is closer to the γ for ice caps, while the c is higher than most. One

possible explanation is that the Coast Mountain glaciers, at the 2004 RGI date of the extent and the thickness models, are in disequilibrium. Therefore, the coefficients may not be representative of steady-state glaciers. In order to account for this uncertainty, a range of coefficient values were used to make a variety of ice load histories, with six c values of 0.0271, 0.0313, 0.0481, 0.055, 0.06861, 0.0728 and four gamma values of 1.140, 1.24, 1.36, 1.497 for a total of 24 ice load histories. The coefficient values were selected to encompass the ranges found in the literature.

For each of the 24 combinations of c and γ values within these ranges, the respective power-law relationship (Equation 3.1) was applied to the LIA glacier areas for the Garibaldi Park region, from Koch *et al.* (2009), to estimate their peak LIA volume. For each coefficient pair, the total LIA volume for the Garibaldi area was then compared to the total volume in the area's glaciers (at 2004) to determine the change from the LIA to 2004 (Figure 3.6). For example, with $c = 0.06861$ and γ= 1.24, the comparison showed that the Garibaldi area's ice volume at the LIA maximum was 220% of the volume at 2004. The percentage increase from 2004 to the LIA for each coefficient pair was then assumed to apply to the entire study region.

Similar to Ice load A, Ice load B begins with the 20 km grid of ice thickness based on Farinotti *et al*. (2019). The solid line profile from Figure 3.4 was used to estimate the glacier change before 2004 (Koch *et al*., 2009). This profile represents relative extent change, assumed to be equivalent to the area. This profile was converted to a volume approximation by applying the power-law relationship for each specific choice of γ and c.

As the ice cylinder centred on each grid area does not change in diameter, the volume change is applied as a height change for each grid area. The profile was scaled as a percent increase based on the volume-area maximum scaled volume increase derived from applying each coefficient pair's respective power-law relationship to the LIA areas in Figure 3.6.

For times later than 2004, the ASTER melt rates from Menounos *et al.* (2018) for 2000-2009 and 2009-2018 were used to project the 2004 estimated thicknesses. Similar to Ice load A, each grid cell in the ice load history has a corresponding thickness determined by each time period's averaged melt rate. The gridded thicknesses for the 2004 time-step were projected forward to a 2009 time-step using the 2000-2009 gridded melt rates and finally to a present-day time-step using the 2009-2018 melt rates.

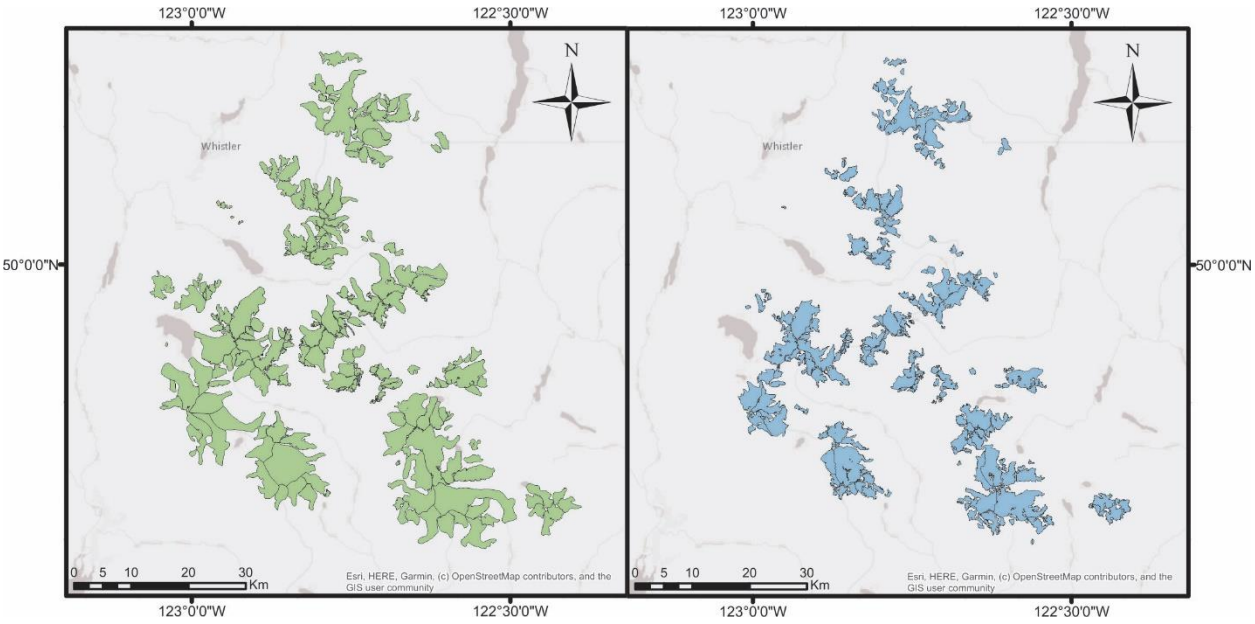

***Figure 3.6**: Garibaldi glacier area (left) at the Little Ice Age maximum extent (Koch et al. 2009), and (right) at present-day (2004) according to the Randolph Glacier Index (RGI Consortium, 2017).*

The total volume over time for each pair of c and γ values is given in Figure 3.7. Any coefficient pair that led to an LIA maximum volume smaller than the 2004 volume was eliminated, leaving 20 ice loading models for consideration. For the 20 remaining ice loading models, larger coefficient values give larger ice volume reconstructions, leading to a wide range of relative LIA maximum volumes between 120% and 460% of the 2004 volume. The LIA maximum volume in the region may have been no more than about 200% of the 2004 volume (B. Menounos, pers. comm., 2021). All the ice volume reconstructions were tested, but the focus in the following is on volumes around 200% (around 1490 km^3) or less.

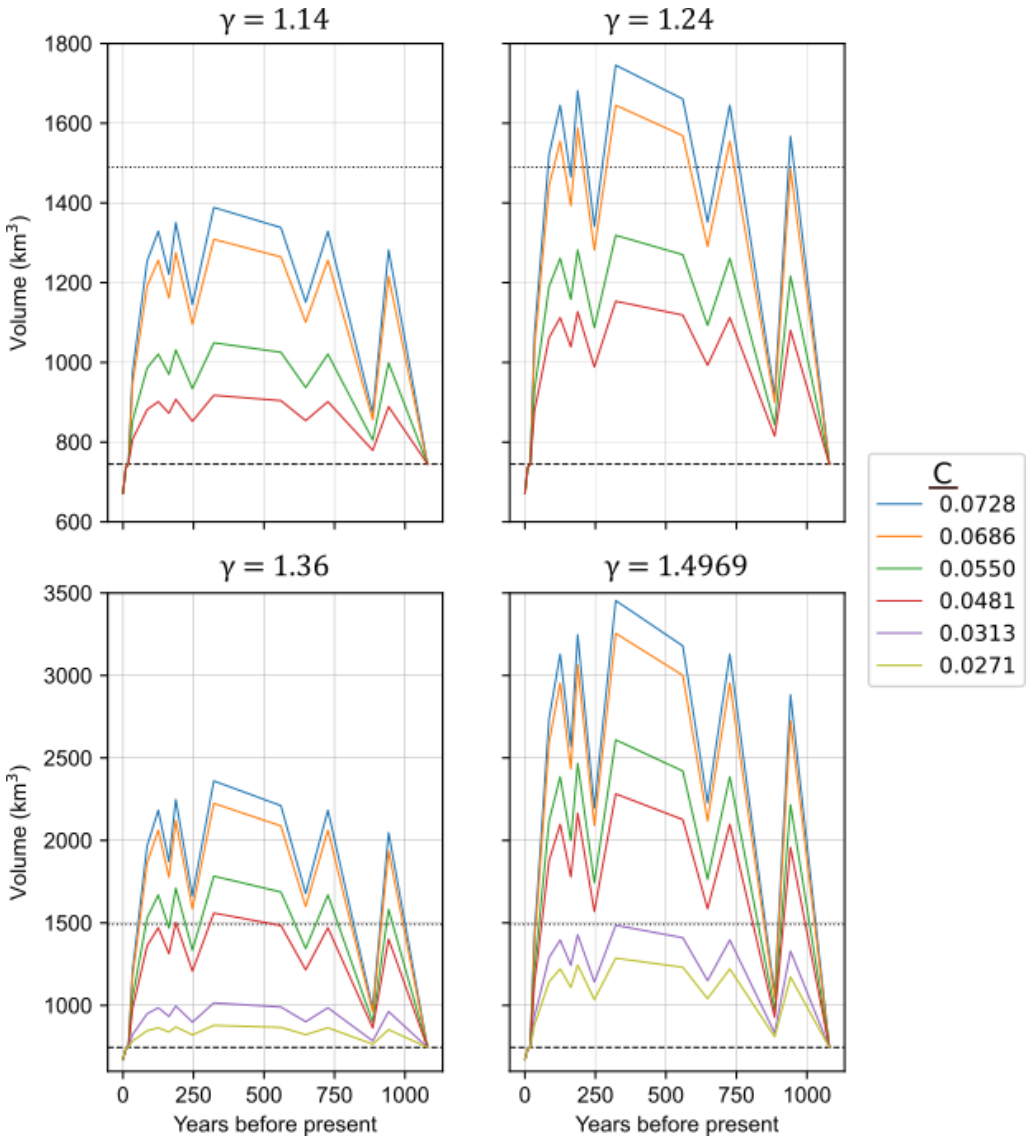

***Figure 3.7**: Total volume through time for each Ice load B combination of γ (separated plots) and c (each line). The black dashed line shows the volume from the Farinotti et al (2018) estimate for the 2004 glaciers. The black dotted line shows the volume that is 200% of the dashed line volume, 1490 km³.*

3.3 Earth Models

The response of the Earth to changes in stress depends on the timescale of the stress. While the lithosphere can be thought of as elastic, bending under stress and then returning to equilibrium once the stress is removed, the mantle layers beneath behave as both an elastic and viscous fluid. Under short time scales (1 to 10^4 seconds) the mantle behaves as an elastic solid, allowing seismic waves (shear and compressional) to propagate with low attenuation. However, on geological time scales of 10^{11} to

10^{17} seconds, the mantle behaves more akin to a viscous fluid (Turcotte and Schubert, 2002). Due to the mantle having both elastic and viscous properties, it is frequently modelled as a viscoelastic fluid. The Earth models used in this study follow the Maxwell model of viscoelasticity, defined as a material where the rate of change of strain is the sum of a linear viscous stress and a linear elastic rate of change of stress:

$$\frac{d\varepsilon}{dt} = \frac{1}{2\mu}\sigma + \frac{1}{E}\frac{d\sigma}{dt} \tag{3.2}$$

Where $\frac{d\varepsilon}{dt}$ is the time rate of change of strain ε, μ is the viscosity, σ is a uniaxial stress, and E is the elastic Young's modulus, for this simplified model of uniaxial stress. Equation 3.2 is the fundamental rheological relation for a Maxwell material (Turcotte and Schubert, 2002). From Equation 3.2, it is possible to see how stress applied over a relatively short period of time allows the elastic strain response to dominate, while a long period of time allows the viscous strain to dominate. GIA models frequently use a Maxwell viscoelastic rheology to accommodate slow flow over thousands of years, as expressed in raised beaches around Hudson Bay, while recognizing the elastic nature of the mantle at short time frames.

The simplified Earth models used in this study have a compressible Maxwell viscoelastic rheology in the mantle, elastic lithosphere, and fluid core. The density and elastic parameters are based on the spherically symmetric Preliminary Reference Earth Model (PREM) containing radially-varying rheological properties of the Earth (Dziewonski and Anderson, 1981). The viscosity profiles follow a variation of the VM5a viscosity structure to allow for variable properties for the top 440 km (the top two layers): an elastic lithosphere with variable thickness, and an asthenosphere layer with variable viscosity (Peltier *et al.*, 2015). The asthenospheric thickness depends on the lithospheric thickness to ensure the sum of the two layers is always 440 km. The three sub-asthenospheric mantle layers have fixed thickness and

viscosity (Figure 3.8). Lithospheric thicknesses are varied between 10 km and 110 km, and asthenospheric viscosity is varied from 1×10^{17} to 5×10^{21} Pa s. Computing the Earth's response to each ice loading history over a wide range of lithospheric thickness and asthenospheric viscosity parameter combinations allow for the determination of the best fitting combination of Earth rheology and ice loading history.

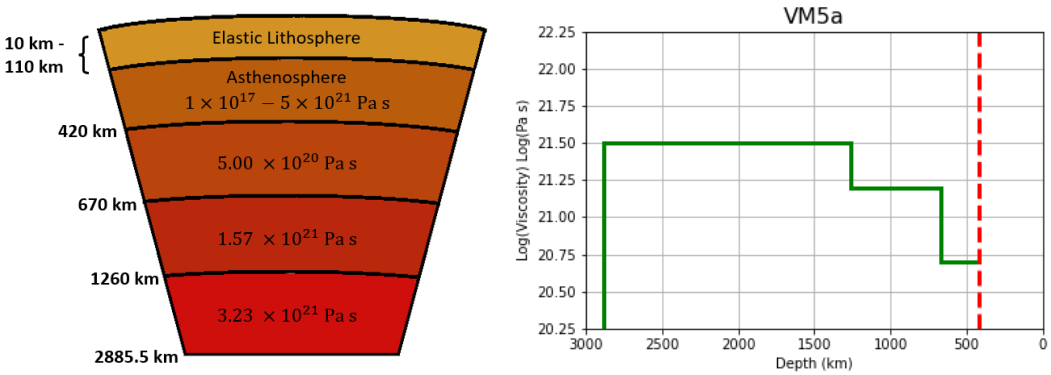

***Figure 3.8**: (Left) Diagram showing Earth model structure used with variable asthenosphere viscosity and lithosphere thickness with VM5a structure below the asthenosphere (Right) VM5a as the green line profile used for the viscosity structure below the asthenosphere (shown as the red dashed line at 420 km depth). Above the red dashed line, the asthenospheric viscosity is variable and the asthenosphere and lithosphere have variable thicknesses, summing to 420 km.*

3.4 GIA Response and GNSS Goodness of Fit

The GIA-induced vertical land motion was predicted for every combination of ice load history and Earth model parameters at the locations of the GNSS stations. The method used for calculating the GIA response is described in James and Ivins (1998).

In order to find the best fitting ice load history and rheology parameter set, the predicted GIA velocities for each ice loading history and Earth model combination are compared to the GNSS observed velocities (see Chapter 2, Table 2.1). The goodness of fit for the modeled velocities compared to the observed velocities is calculated using a normalized RMS statistic (NRMS):

$$NRMS = \sqrt{\frac{\sum_{i=1}^{i=N}\left(\frac{f_{obs,i} - f_i}{\sigma_i}\right)^2}{N}}$$

Where f_i and $f_{obs,i}$ are the model output velocity and the observed GNSS velocity at each GNSS station, i, respectively, σ_i is the error at each GNSS site and N is the number of sites.

Chapter 4: Results and Discussion

4.1 Introduction

Following the methods described in section 3, Ice load A and all variants of Ice load B were combined with Earth models containing a range of lithospheric thicknesses and asthenospheric viscosities to predict vertical crustal motion in the Coast Mountains region. This section outlines the results of the GIA modelling and how these predicted uplift rates, for each parameter combination, compare to the GNSS vertical velocities described in Chapter 2. The GNSS vertical velocities were then corrected for modelled interseismic crustal motions and residual crustal uplift from GIA generated by the Cordilleran Ice Sheet during the last full glacial cycle to determine their effect on the best fitting Earth rheology parameters. These best fitting parameters are compared to the asthenospheric viscosities and lithospheric thicknesses in previous studies in southwestern BC as well as tectonically active areas like Southeast Alaska and Patagonia. Finally, the model shortcomings are discussed and possible improvements to future GIA modelling in the Coast Mountains area are suggested.

4.2 Ice load A

The Ice Load history A was used in 715 model runs, each with a unique Earth model representing a different combination of lithospheric thicknesses (13 values ranging from 10 to 110 km) and asthenospheric viscosities (55 values ranging from 10^{17} Pa s to 10^{21} Pa s). The spatial pattern (width) and peak magnitude of the predicted uplift rates vary with the parameter values.

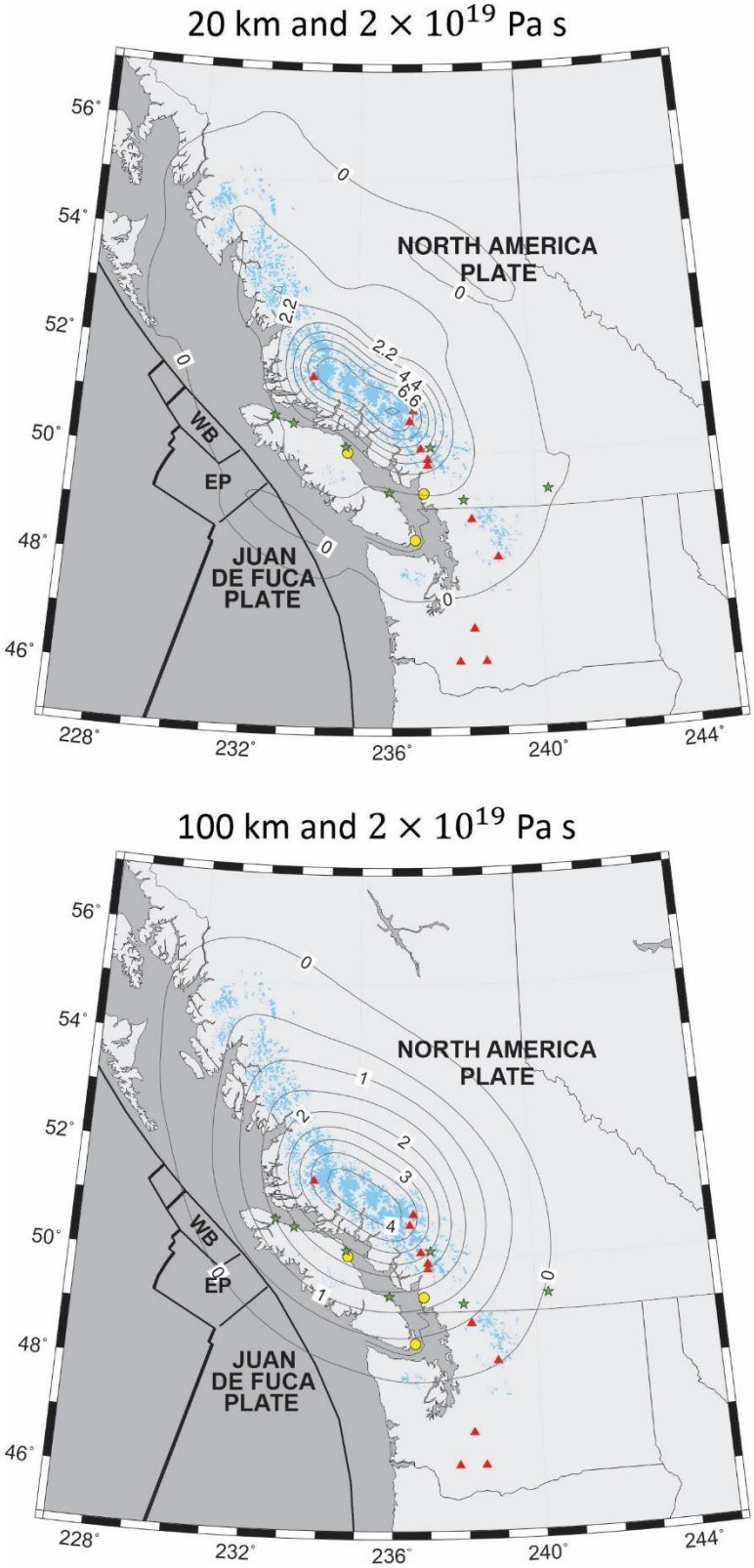

Figure 4.1: *Contours of predicted uplift rates (in millimetres per year) for Ice load A. The Earth model has a fixed asthenospheric viscosity of 2×10^{19} Pa s with (top) 20 km thick lithosphere and (bottom) 100 km thick lithosphere.*

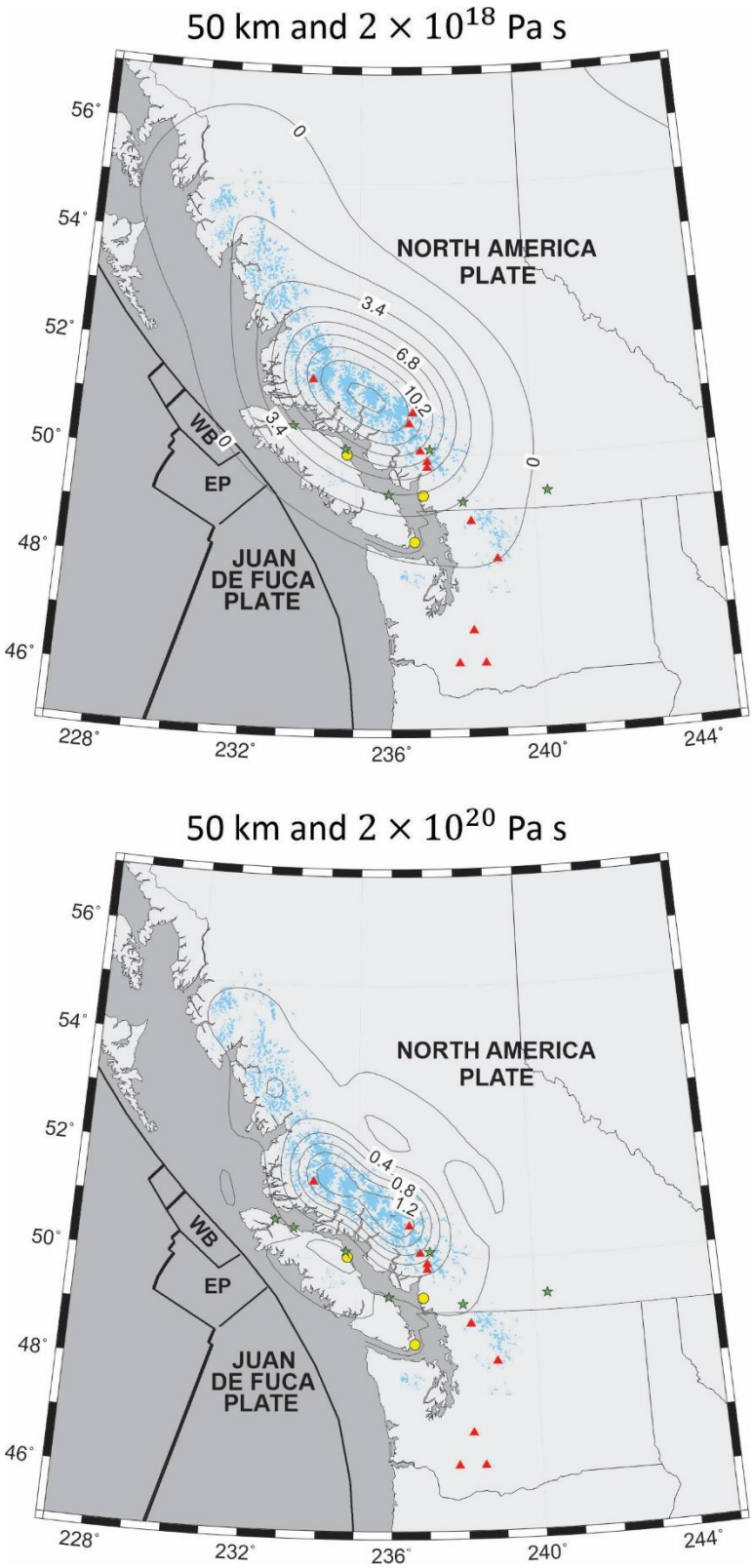

***Figure 4.2**: Modeled uplift contours for Ice load A ice history, with fixed Lithospheric thickness of 50 km with (top) asthenospheric viscosity of 2×10^{18} Pa s and (bottom) asthenospheric viscosity of 2×10^{20} Pa s.*

Figure 4.1 presents two examples of the model predicted uplifts, where the lithospheric thicknesses are 20 km and 100 km, and the asthenospheric viscosity is held constant at 2×10^{19} Pa s. The region with uplift larger than 2 mm yr^{-1} is distributed over a larger area for the 100 km thick lithosphere model and has a maximum uplift contour of 4 mm yr^{-1}, compared to 8 mm yr^{-1} for the much thinner 20 km thick lithosphere. The differences in the magnitude and pattern of predicted uplifts are due to the thicker lithosphere supporting more of the ice load and having a greater flexural rigidity (James *et al*., 2000, 2005; Turcotte and Schubert, 2002). The thicker the lithosphere, the more it resists bending under the applied ice load.

Variations in the asthenospheric viscosity, shown in Figure 4.2, also dramatically affect the modeled uplift pattern and magnitude. For a fixed lithospheric thickness of 50 km the 2×10^{20} Pa s asthenosphere produces much smaller uplift rates (around 1.4 mm yr^{-1} maximum), while the 2×10^{18} Pa s asthenosphere predicts a peak uplift rate of more than 12 mm yr^{-1}. The higher viscosity asthenosphere resists deformation more than the lower viscosity asthenosphere. Ice Load A features a uniform ice thickness decrease for the past 300 years (see Figure 3.3), and the 2×10^{18} Pa s asthenosphere responds much more to the load change over this relatively short timespan than the 2×10^{20} Pa s asthenosphere.

This can be understood by estimating the relaxation times for the two different viscosities using Equation 1.2. The wavelength, λ, for the load can be estimated to be about 200 km (half the width of the LIA ice load) and the constants ρ and g are 3300 kg m^{-3} and 9.8 m s^{-2} (Turcotte and Schubert, 2002). This leads to a relaxation time of around 123 years for the 2×10^{18} Pa s asthenosphere, and 12,300 years for the 2×10^{20} Pa s asthenosphere. Considering the difference in magnitudes between both relaxation times, it is clear that an asthenosphere on the order of 10^{20} Pa s will not respond to the recent LIA ice load changes as to the same degree as the lower 10^{18} Pa s and even 10^{19} Pa s asthenosphere models. While these calculations of relaxation time are not precise, they do offer insight into possible upper

limits for viscosities. For more robust analysis, the modelled results are compared to the GNSS observed vertical velocities from section 2.

The uplift rate was calculated at each GNSS site location for each Earth model parameter pair and compared to the observed uplift rates. Figure 4.3 presents a contour plot of the goodness of fit normalized root-mean-square (NRMS) values for lithospheric thickness and asthenospheric viscosity. With correctly estimated uncertainties and a model that fits the observations, the NRMS value would be 1. As this would be an ideal case and would require the model to be representative of all degrees of freedom of the system, the best fitting model has an NRMS closest to 1. For Ice Load A the minimum NRMS found was 7.5 for 50 km thick lithosphere and a 2×10^{19} Pa s asthenospheric viscosity. Asthenospheric viscosity is well constrained by the observations to be close to the minimum value, but a broad range of lithospheric thicknesses satisfy the observations nearly as well as the 50 km thickness of the minimum NRMS. This is best seen by the bold white line on Figure 4.3 for the NRMS of 10.5. The 10.5 contour contains every possible lithospheric thickness while only containing a small range of viscosities.

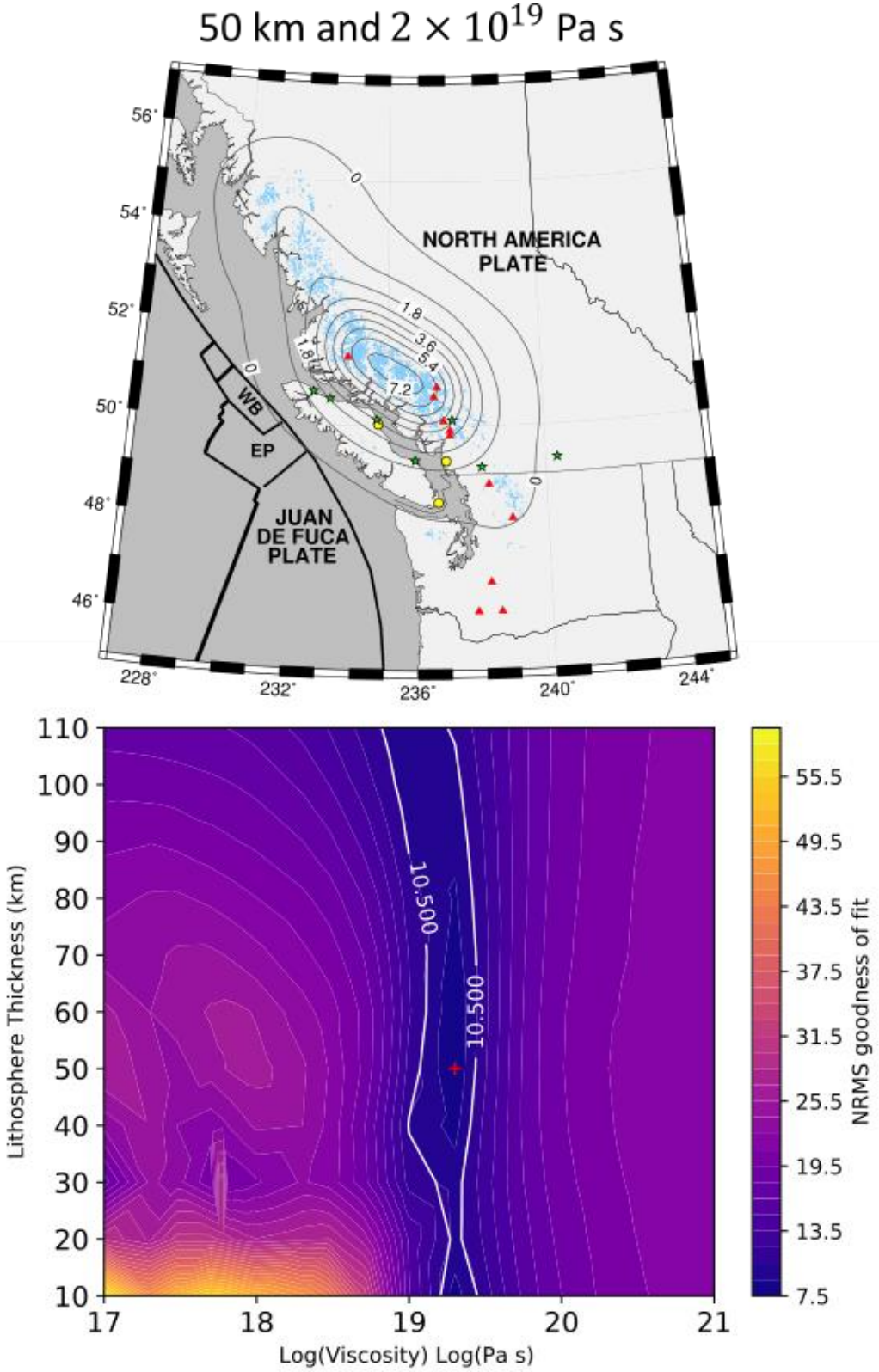

***Figure 4.3**: (top) Modeled uplift for best fitting set of model parameters with Ice load A: 50 km thick lithosphere and 2×10[19] Pa s asthenospheric viscosity. (bottom) Contour plot of all tested model parameters and their respective goodness of fit with a red plus to denote the lowest NRMS value's location. The white line for NRMS 10.5 shows the lack of sensitivity for lithospheric thickness.*

4.3 Ice Load B

Ice Load B, as described in section 3, follows the ice change timing from Koch *et al.* (2007), shown in Figure 3.4. The magnitude of the volume change is based on the glacier volume-area scaling relationship, Equation 3.1, and referenced to the Garibaldi area change between 2004 and the LIA maximum (Koch *et al*., 2009; Bahr *et al*., 1997). A range of volume-area scaling relationships were created by selecting a range of both scaling parameters, c (the multiplicative scaling factor) and γ (the volume-area scaling exponent).

With the additional unknowns of c and γ, 20 ice load histories were created (after filtering out any combinations of c and γ that result in lower maximum volume than the starting volume, as described in Chapter 3). Model predictions were generated using each Ice Load B and the 715 Earth models, to span the range of lithospheric thicknesses and asthenospheric viscosities, similar to Ice Load A. The best fit was computed for each set of c and γ to find the optimal pair of lithospheric thickness and asthenospheric viscosity for each of the 20 ice loads.

Table 4.1 Minimum NRMS value, asthenospheric viscosity, effective elastic lithosphere thickness, c value, γ value, and the maximum volume of the best fit for each ice load history's 715 model runs

NRMS	Asthenospheric Viscosity (Pa s)	Lithospheric thickness (km)	c	γ	Maximum Volume (km^3)
5.557	3.0×10^{19}	55	0.05500	1.4969	2609
5.730	2.0×10^{19}	45	0.04810	1.4969	2282
5.734	1.0×10^{19}	45	0.07280	1.1400	1388
5.734	2.0×10^{19}	45	0.06861	1.3600	2224
5.789	8.5×10^{18}	45	0.06861	1.1400	1308
5.825	8.5×10^{18}	45	0.05500	1.2400	1318
5.900	1.0×10^{19}	45	0.03130	1.4969	1485
5.956	6.0×10^{18}	45	0.04810	1.2400	1153
5.977	7.5×10^{18}	45	0.02710	1.4969	1285
6.049	2.0×10^{18}	40	0.04810	1.1400	917
6.070	2.0×10^{18}	45	0.02710	1.3600	878
6.087	3.0×10^{18}	40	0.03130	1.3600	1014
6.128	3.0×10^{19}	60	0.07280	1.3600	2360
6.191	5.0×10^{18}	45	0.05500	1.1400	1049
6.312	1.0×10^{19}	40	0.04810	1.3600	1559
6.336	5.0×10^{19}	70	0.07280	1.4969	3453
6.340	3.0×10^{19}	45	0.06861	1.4969	3255
6.414	2.0×10^{19}	55	0.05500	1.3600	1783
6.461	2.0×10^{19}	55	0.07280	1.2400	1745
7.188	2.0×10^{19}	60	0.06861	1.2400	1645

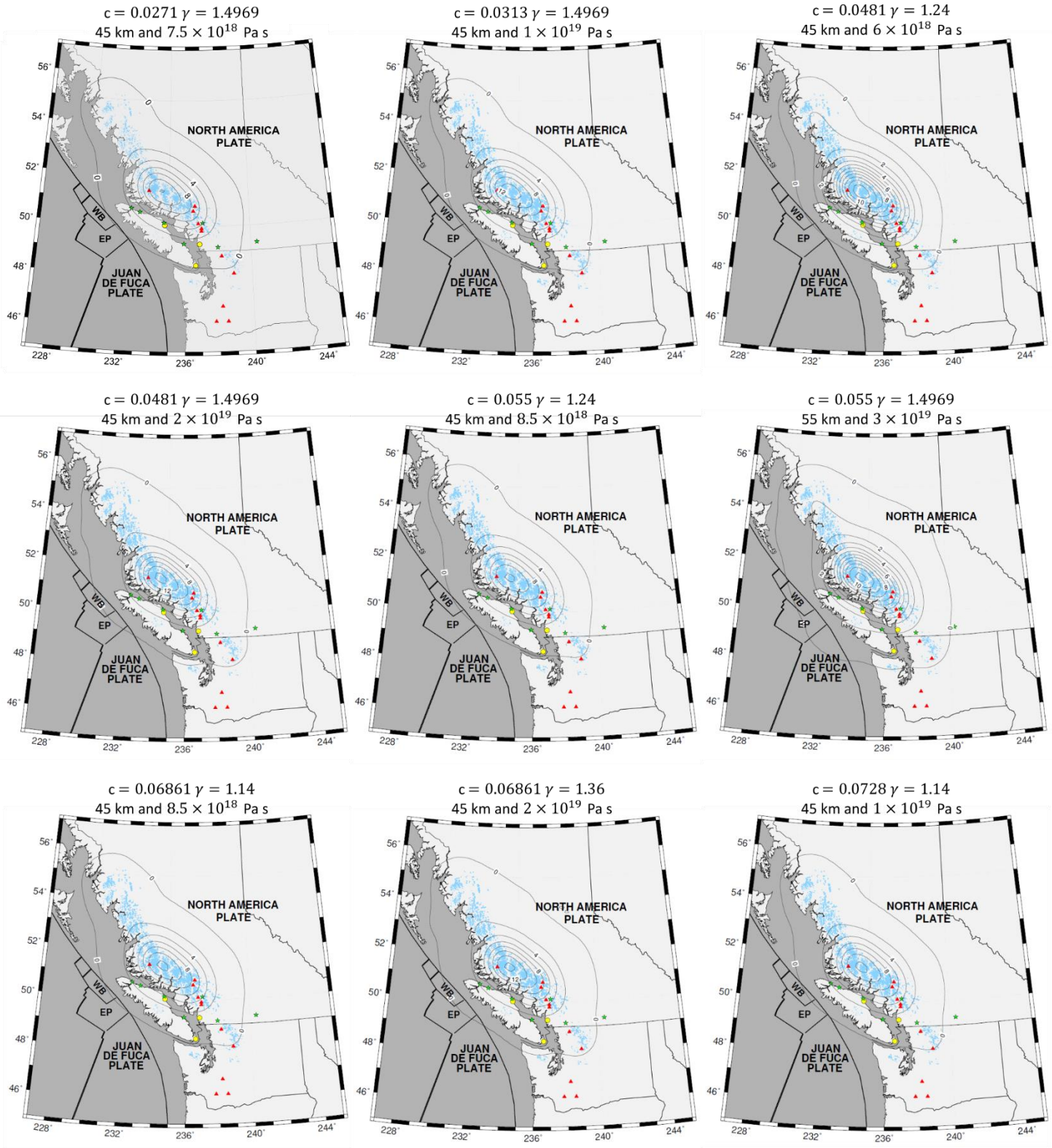

***Figure 4.4**: Modeled uplift for the 9 best fitting Ice Load B volume-area scaling relationships and their respective best fit model parameters.*

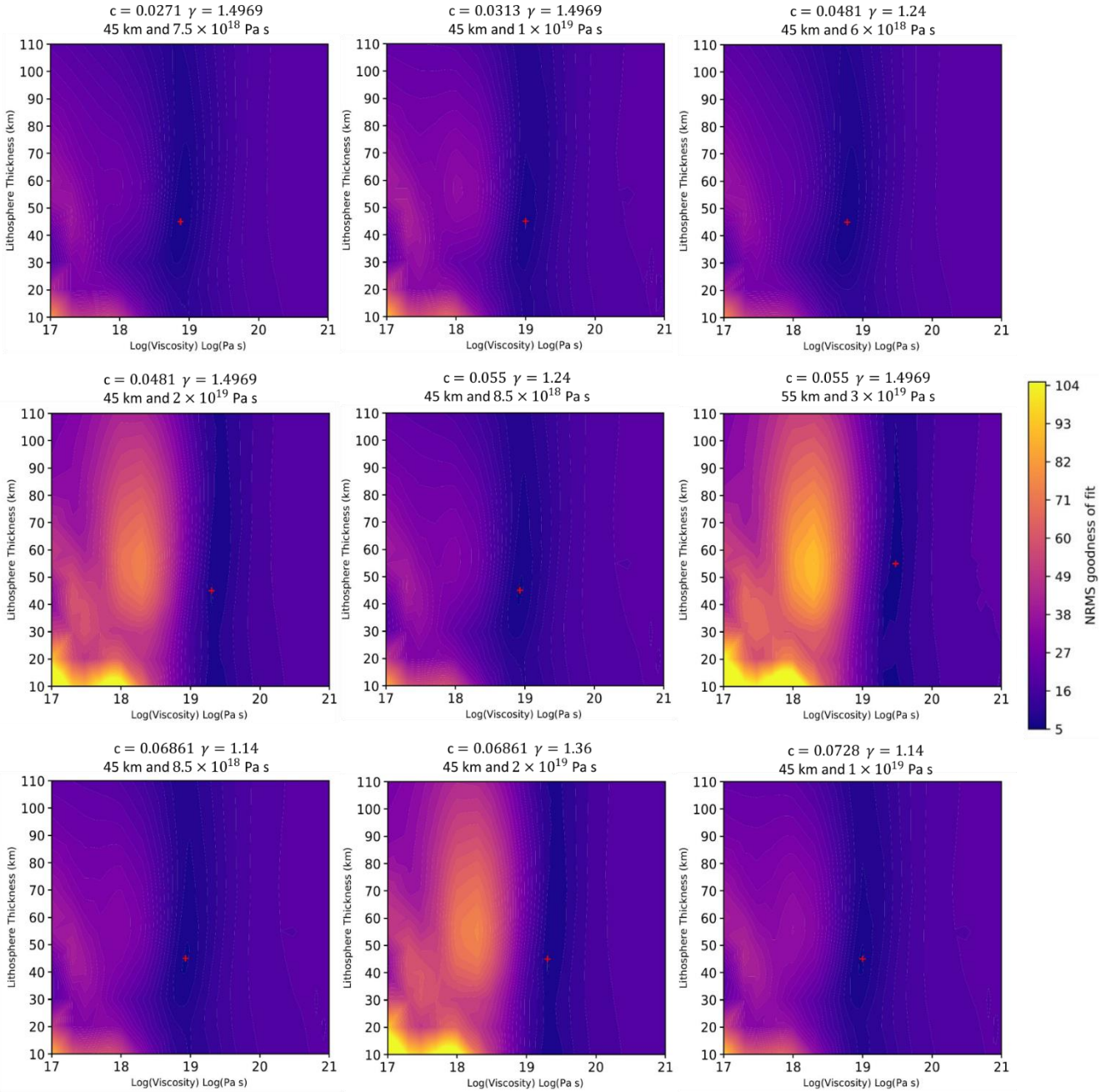

Figure 4.5: *Goodness of fit contour plots for each of the 9 best fit Ice load B ice histories. The red plus denotes the lowest NRMS value.*

Figure 4.4 presents the predicted uplift rates for the best fitting parameter combinations for each ice load model run. Only the models that produced NRMS values below 6 are included. The full span of lowest NRMS values ranged from around 5.5 to 7.2, as shown in Table 4.1. The ice load with the c and γ

pair empirically derived in section 3.2.2 (c = 0.06861 and γ = 1.24) had the highest minimum NRMS value of all the tested pairs, 7.188.

Maximum predicted uplifts range between 10 mm yr^{-1} and 14 mm yr^{-1}, while the spatial pattern of predicted uplift rates remained relatively consistent due to the small range in lithospheric thicknesses (45-55 km). Figure 4.5 shows the NRMS contour plot for the same nine best-fit load histories shown in Figure 4.4, along with the location of their respective NRMS minima. The asthenospheric viscosity is well constrained and the best fitting ranges from 6×10^{18} Pa s to 3×10^{19} Pa s for all 9 models shown. However, lithospheric thickness is less constrained around the lowest NRMS parameter combinations, shown in the elongated vertical bands of low NRMS around the best fitting values in Figure 4.5.

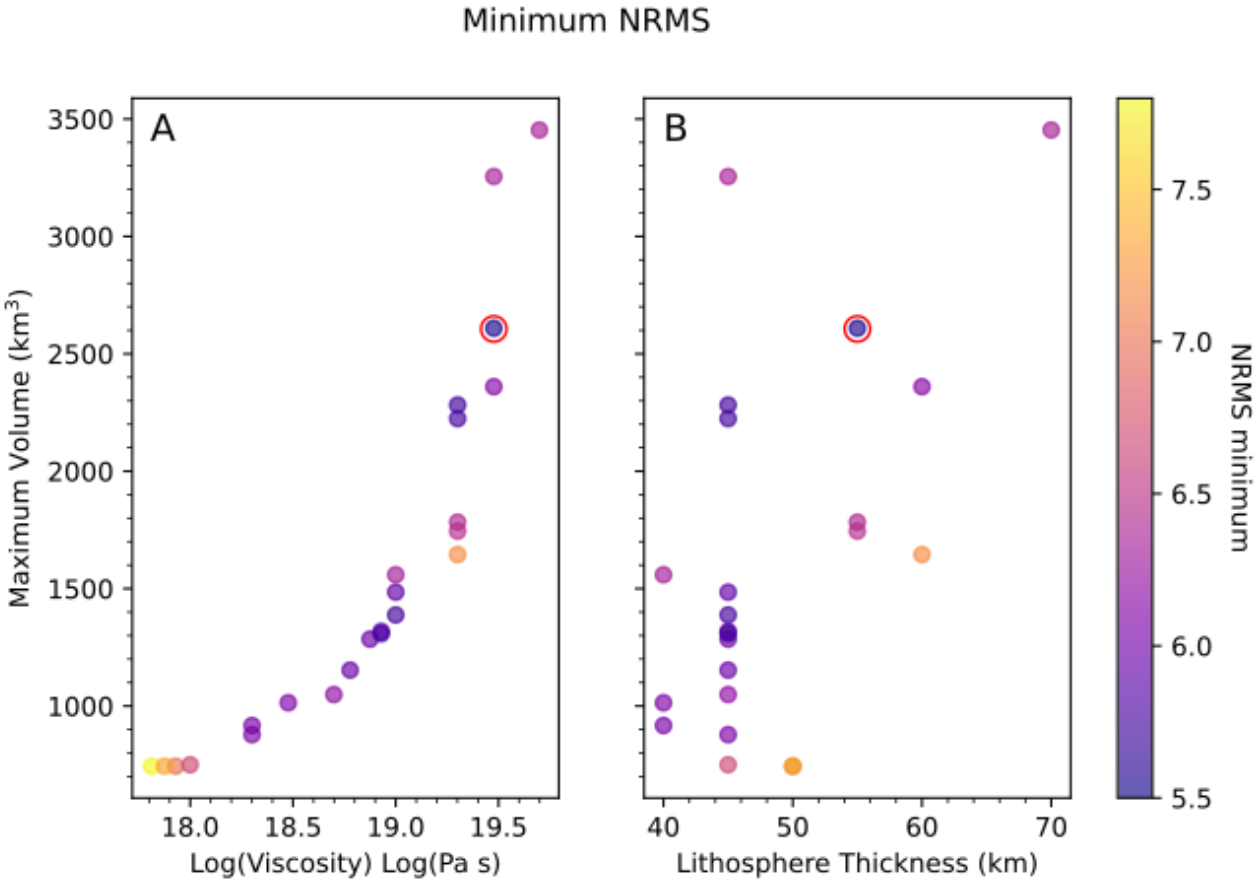

Figure 4.6*: Locations of NRMS minimum for each Ice load B parameter set for (A) maximum ice load volume versus log(viscosity), and (B) maximum ice load volume versus Lithospheric thickness. Color bar on the right shows the scale of the NRMS value plotted in each plot, and the red circles represent the absolute lowest NRMS of the entire test*

To explain the differences between each ice load and better understand why there is a range in best fitting earth model parameters, Figure 4.6 shows the best fitting parameters in terms of maximum ice load volume. While Figure 3.7 shows that each c and γ pair vary in the magnitude of ice volume changes, focusing on the maximum volume helps analyze how the different ice loads lead to different optimal parameters. Figure 4.6 shows the ice load's minimum NRMS's in terms of asthenospheric viscosity versus maximum volume and lithospheric thickness versus maximum volume. Figure 4.6A shows a clear trend for the best fits in terms of asthenospheric viscosity and maximum volume. This trend fits well with the theory discussed in section 4.2 for how the higher viscosity asthenosphere resists deformation more than a lower viscosity asthenosphere. Therefore, if the asthenosphere has a higher viscosity, only the larger ice load volumes can create the responses that best match the observations. In contrast, Figure 4.6B shows a less clear trend in best fits with lithospheric thickness versus maximum volume. However, Figure 4.6B does show that in order to fit the response to lithospheres thicker than 45 km the maximum ice volume must be much larger. This supports the conclusions of James and Clague (2002), outlined in section 1.8, that a thicker lithosphere supports more load through its flexural rigidity, and so recreating the observed response requires a larger peak ice volume, in this case above 1600 km^3.

An example of the difference between maximum volumes is shown in Figure 4.7, showing predicted uplifts from ice loads with maximum volumes of 1308 km^3 (c = 0.06861 and γ = 1.14) and 2609 km^3 (c = 0.055 and γ = 1.4969). Each model run shown has the same earth model parameters of 10^{19} Pa s asthenospheric viscosity and 45 km thick lithosphere.

Overall, varying all three parameters (maximum ice volume, lithospheric thickness, and asthenospheric viscosity) led to very similar uplift patterns to best fit the observational data. The range of peak uplifts of the 9 best fitting ice load models, shown in Figure 4.4, lie between 10 and 14 mm yr^{-1} despite differing maximum ice volumes. The best fitting earth model parameters differed to compensate for the changes in ice load magnitude and create a tight range for possible uplift patterns. Therefore, the model predicts

that the region likely has a peak uplift within this 10-14 mm yr^{-1} range, independent of the three variables.

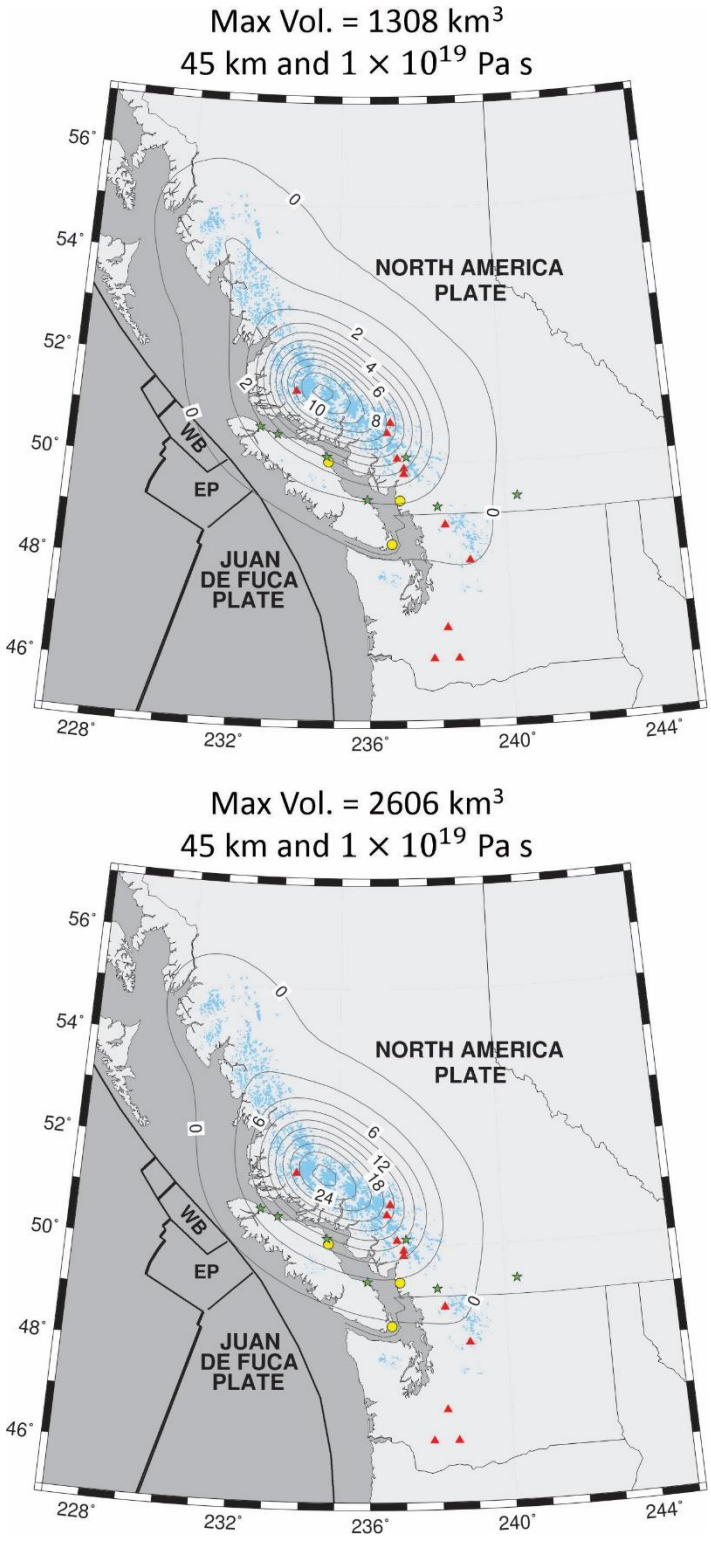

***Figure 4.7**: Contours of predicted uplift rates for two different Ice Load B versions, (top) with maximum volume of 1308 km³ and (bottom) with maximum volume of 2606 km³. Both plots have lithospheric thickness of 45 km and asthenospheric viscosity of* 10^{19} *Pa s.*

4.4 Effect of Corrections to Observed Uplift Rates

Section 2.2 discussed other potential sources of the uplift signal in the study area not related to GIA. The analysis described in sections 4.2 and 4.3 did not correct for possible modelled interseismic uplift from Li *et al.* (2018). Here we consider the modelled interseismic vertical signal from the Li *et al.* (2018) model, with vertical deformation rates taken from Yousefi *et al.* (2020).

In addition, we apply a possible correction for last glacial maximum GIA. In order to capture residual GIA from the last glacial maximum two GNSS sites located in the interior of BC were chosen and their vertical velocities were averaged. WILL, located near Williams Lake BC, and DRAO, in Penticton BC, were chosen due to their relatively small, but non-zero, uplift rates and their positions away from the Coast Mountains. It was assumed that the average vertical velocity between these two sites would be a good estimate of the Cordilleran Ice Sheet GIA signal. WILL and DRAO have vertical velocities of 1.77 mm yr^{-1} and 0.49 mm yr^{-1} respectively, with an average of 1.13 mm yr^{-1}. The observed and corrected GNSS vertical velocities are presented in Table 4.2, along with the interseismic correction and the LGM correction.

Table 4.2: The seven GNSS sites used in the NRMS comparison with their respective modeled interseismic vertical velocity from Yousefi et al. (2020). The final corrected GNSS vertical velocities also have the assumed 1.13 mm yr^{-1} from the LGM residual uplift.

GNSS site	Modeled interseismic vertical velocity (mm yr^{-1}) from Yousefi *et al.,* (2020)	Estimated Residual LGM GIA (mm yr^{-1})	Original Observed GNSS (mm yr^{-1})	Corrected GNSS vertical velocity (mm yr^{-1})
BCPH	-0.654	1.13	2.53	2.054
BCOV	-1.153	1.13	2.38	2.403
QUAD	-2.002	1.13	4.11	4.982
NANO	-0.842	1.13	1.01	0.722
WSLR	-1.529	1.13	4.25	4.649
CHWK	-1.628	1.13	1.77	1.218
DRAO	-1.00	1.13	0.72	0.360

As in section 4.3, the best fit was computed for each variant of Ice Load B, corresponding to each set of c and γ, to find the optimal pair of lithospheric thickness and asthenospheric viscosity for each of the 20 ice loads. Table 4.3 shows the 9 lowest NRMS fits arising from the comparison with the corrected GNSS vertical velocities. The lowest NRMS values are larger than their uncorrected counterparts. Further, the corrected GNSS velocities fit with slightly lower lithospheric thicknesses ranging from 40 km to 45 km, and the range of asthenospheric viscosities shifts towards lower values, moving the lower bound from 6×10^{18} Pa s to 5×10^{18} Pa s and the upper bound from 3×10^{19} Pa s to 2×10^{19} Pa s. Although the corrections shifted the resulting lithospheric thicknesses and asthenospheric viscosities to slightly lower ranges, the corrected NRMS values were larger than the NRMS for the uncorrected GNSS velocities.

Table 4.3: Minimum NRMS value, asthenospheric viscosity, effective elastic lithosphere thickness, c value, γ value, and the maximum volume for the best 9 ice load history's 715 model run results that best fit the corrected GNSS vertical velocities

NRMS	Asthenospheric Viscosity (Pa s)	Lithospheric thickness (km)	c	γ	Maximum Volume (km^3)
7.460	2×10^{19}	45	0.04810	1.4969	2282
7.495	8.5×10^{18}	40	0.07280	1.1400	1388
7.512	2×10^{19}	45	0.06861	1.3600	2224
7.527	1×10^{19}	40	0.04810	1.3600	1559
7.530	7.5×10^{18}	40	0.06861	1.1400	1308
7.558	7.5×10^{18}	40	0.05500	1.2400	1318
7.559	9×10^{18}	40	0.03130	1.4969	1485
7.650	5×10^{18}	40	0.04810	1.2400	1153
7.652	2×10^{19}	40	0.07280	1.3600	2360

4.5 Comparisons to Previous GIA Modelling

The results of this study can be compared to those of previous GIA studies in southwestern BC, as well as other tectonically active regions such as southeast Alaska and Patagonia. The range of best fitting earth model parameters from Ice load B (ice loads with NRMS values below 6) overlaps with previous

studies' results (Figure 4.8). As discussed in section 1.6, Yousefi *et al.* (2018) modeled GIA in the region from Cordilleran ice sheet retreat. Including the best fitting model results and the data weighted model results, they found the asthenospheric viscosity was between 5×10^{18} to 5×10^{19} Pa s, with a lithospheric thickness of 46 km (Yousefi *et al*., 2018). James *et al.* (2009) employed a fixed lithospheric thickness of 60 km corresponding to the depth to the top of the subducting slab below the Strait of Georgia (James et al., 2009b). The GIA model results from James *et al.* (2009) found that the optimal asthenospheric viscosity ranges from 3×10^{18} to 4×10^{19} Pa s, depending on the asthenospheric thickness (James et al., 2009b).

GIA model results from southeast Alaska and Patagonia are also helpful for comparison due to their proximity to active tectonic margins. Southeastern Alaska is in the proximity of the same transform fault system that lies to the west of the Central Coast Mountains. Hu and Freymueller (2019) modeled GIA for Southeast Alaska and northwestern Coastal BC for ice change over the last 2000 years. Earth models followed the VM5a viscosity structure with varied lithospheric thickness and asthenospheric viscosity, and predictions were compared to GNSS uplifts. The authors found that the best fitting parameters fit within 2-5×10^{19} Pa s and lithospheric thicknesses range from 45 to 70 km (Hu and Freymueller, 2019).

Patagonia is in a seismically active zone due to the proximity of a major subduction zone to the west. The area experienced significant ice mass loss since its own LIA maximum (Dietrich *et al*., 2010). Lange *et al.* (2014) found that the northeastern edge of the Southern Patagonia Icefield experienced vertical crustal uplift of 39 mm yr^{-1} due to GIA. The authors conducted a similar search for optimal lithospheric thickness and asthenospheric viscosity to match the observed uplift from GNSS observational data. It was found that a viscosity range of 1.6-8×10^{18} Pa s along with a lithospheric thickness of 36.5 km (±5 km) was optimal for matching GNSS uplifts in the area (Lange *et al*., 2014).

Figure 4.8 shows a comparison of the best fitting model parameters found in this study with those of the previous studies outlined above. The uncorrected Ice Load B results overlap with the works of Yousefi *et al.* (2018) and Hu and Freymueller (2018). James *et al.* (2009) is shown as a straight line due to the fixed 60 km lithospheric thickness, but its resulting asthenospheric viscosity range encompasses the ranges of both Ice Load B tests as well as Ice Load A. Finally, Lange *et al.* (2014) found lower lithospheric thicknesses and asthenospheric viscosities but the upper bounds of both parameters approach those of Ice Load B (corrected more than the uncorrected). The GIA models presented in this study agree well with the trends seen in the previous work in other, similar areas. As this study focuses on a different area than the works discussed in this section, different results are expected.

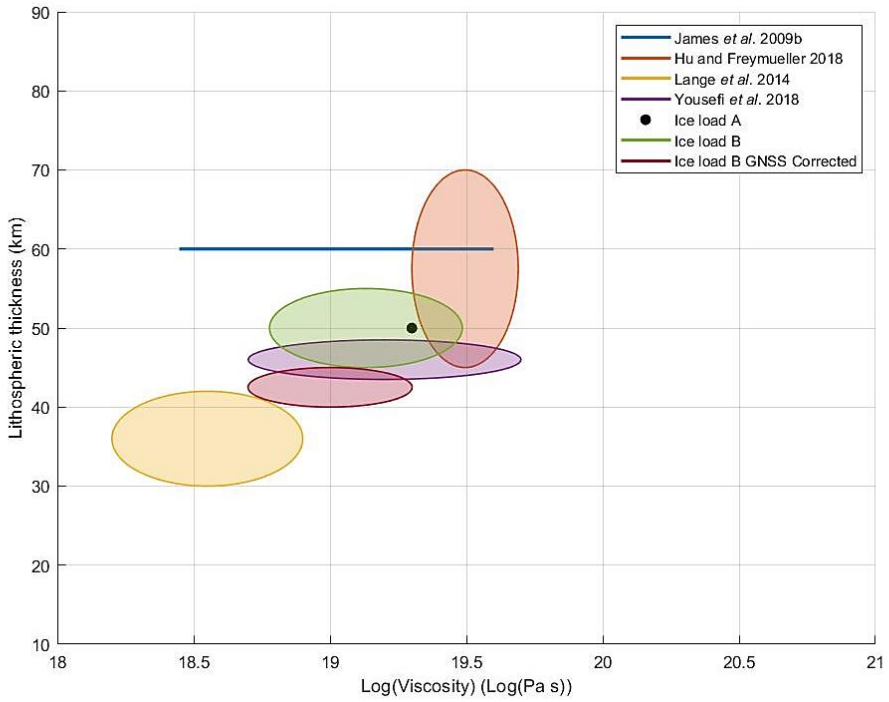

Figure 4.8*: Plot of Lithospheric thickness versus log(viscosity) ranges found by previous studies on GIA in southwestern BC area (blue line, James et al. 2009b and purple, Yousefi et al. 2018), the adjacent area of Southeast Alaska/northwestern coastal BC (orange, Hu and Freymueller 2018), and the tectonically similar Patagonia region (yellow, Lange et al. 2014). For comparison, the best fitting parameter set for Ice load A (black dot) and the parameter range for both the uncorrected (green) and corrected (dark red) Ice load B are also plotted.*

4.6 Potential Sources of Uncertainty and Areas for Future Model Improvement

While results of this study show good agreement with the GIA models discussed in section 4.5, the minimum NRMS values were between 5.5 and 8. This indicates that there are misfits between the GIA model predictions and GNSS vertical velocities, even for the best fitting models. This could be due to either the GNSS errors being too optimistic, or that there remain uncertainties within the model that cause a systematic mismatch. Within the model, there are uncertainties that arise due to the ice loads, the earth models, and the modelling approach that affect the fit of the predictions to the observed uplift. Additionally, the model accuracy could be improved with additional GNSS stations, one additional GNSS station within the area of maximum uplift, or the inclusion of additional uplift datasets (such as levelling line surveys). In this section I will discuss some of the uncertainties and assumptions in this study, as well as some suggestions on how to address these issues and improve model fit and accuracy.

4.6.1 Ice History

The ice load histories employed in this study have a number of simplifying assumptions and further work could be done to develop an ensemble of Coast Mountain glacier evolution models for input to surface loading calculations. Ice Load A is discussed in section 3.2; it involves extrapolating a flat rate of ice mass loss back 300 years which is a simplifying assumption. Ice Load B improves slightly on this by using a profile of ice extent over time and proportionate ice thickness changes based on volume-area scaling. However, these add new uncertainties to Ice Load B. The ice extent profile is treated as a qualitative guide for proportionate ice changes. Furthermore, it is a history profile for only the Garibaldi Park region, one area among many in the Coast Mountains. The timings for ice change are accepted to be largely synchronous across much of the region (Menounos *et al*., 2009); however, the magnitude may differ drastically between areas, particularly with changes in latitude and elevation. The Coast Mountains contain major icefields such as Ha-Iltzuk Icefield, which hold much larger ice masses than the Garibaldi region. Basing the ice load changes solely on Garibaldi region glaciers could lead to significant

bias towards the changes of smaller ice masses, as the growth and decay experienced by the Garibaldi region glaciers is assumed to be proportionately the same for the entire study region.

Additionally, the application of the volume-area scaling comes with its own set of assumptions. While a range of scaling exponents was tested, it is typically accepted that γ should be a constant and that the multiplicative scaling parameter, c, varies between individual glaciers and over time (Bahr *et al.*, 2015). The volume-area scaling relationship remains a good way to estimate glacier volumes. However, an improved Ice load B could keep γ = 1.36 as a constant and instead test the temporal and spatial variability of c to find the best fit. One improvement, at least to the spatial variability of c, could come from more *in situ* measurements of LIA glacier extents in other parts of the Coast Mountains to produce representative maps (such as those from Figure 3.6) to estimate c for many of the subregions in the study area.

Explicit modelling of the evolution of Coast Mountain glaciers and ice fields, driven by an ensemble of past climate reconstructions (temperature, precipitation) would provide an improved representation of the surface-loading component of future GIA modelling of the region. One of the most promising methods that could be used for estimating glacier change into the past is the Open Global Glacier Model (OGGM). OGGM is an open-source modelling framework that can simulate past and future glacier extent/geometry and volume of individual glaciers (Maussion *et al.*, 2019). It is a powerful tool for predicting ice changes due to various climate models. Coupled with suitable historical climate models, OGGM could be used to estimate glacier changes since the LIA. One of the tools developed in conjunction with OGGM is the initialization system. Due to the lack of extensive *in situ* data and empirical evidence of past glacier parameters, it is difficult for any model to accurately project into the past as it becomes an inverse problem and leads to non-unique solutions for glacier initial states (Eis *et al.*, 2019). The initialization tool of OGGM generates a large number of physically plausible past initial glacier states and then models them forward in time to the present. The modeled present glaciers are

compared to the observed present glaciers, and the best 5% are taken. This initialization could be applied to each glacier in the Coast Mountains study area. However, this is very computationally expensive due to the number of glaciers and the number of initial states needed to get an accurate result. Still, it remains promising for a much more accurate ice loading history for future GIA modelling.

4.6.2 New GNSS Sites and other sources of vertical land motion observations

Only seven GNSS sites were used to provide the observational data, and of those seven sites, only one (WSRB) is located within an area with ice mass change. Additional GNSS sites at critical locations would improve the accuracy of the model. Ideally, one or more additional GNSS sites within the area of maximum predicted uplift would allow for a massive improvement in accuracy, as Figure 4.4 shows that even among the best fitting model results, there is variation in maximum uplift. Currently the best fitting models have maximum uplifts between 10 mm yr^{-1} and 14 mm yr^{-1}, but a GNSS site located in this area of maximum GIA response would greatly reduce this range and be invaluable to further constrain the rheological parameters. Other GNSS sites would constrain the spatial pattern of uplift and potentially provide additional constraints on effective lithospheric thickness and glacial load history.

Another way to improve observations is to look at other sources of data, such as levelling surveys. From 1927 to 1993, several levelling surveys have been conducted along a line between Horseshoe Bay and Lillooet, BC. This line is located close to areas of ice change, similar to WSRB, and could be used to constrain the model unknowns further. The levelling provides information along a levelling line that relates to the amount of crustal uplift over past decades corresponding to when the line was levelled and relevelled. In contrast, GNSS provides measurements of crustal uplift over recent years, and at selected sites, for up to the past three decades. Tide gauge observations are subject to a large number of oceanographic effects, as well as subject to vertical land motions, but a comprehensive investigation would include examination of tide gauge time series for evidence of vertical land motions and their possible changes over time.

4.6.3 Tectonic Setting and Lateral Heterogeneity

Section 1.6 outlines the evidence for lateral heterogeneity in lithospheric thickness and asthenospheric viscosity, particularly when comparing the Coast Mountains study region to the stable continental craton of the Hudson Bay region. However, there is also Earth heterogeneity within the study region. The assumption of lateral homogeneity in the Earth models, in a region with significant lateral heterogeneity, may introduce biases into inferred best-fitting model parameters. As well, we have considered a linear viscoelastic rheology. Future work could consider non-linear and transient rheologies, which may be particularly important to evaluate if the ice load change accelerates with time.

Figure 1.9 shows the map of heat flow for southwestern BC. Note the areas with high heat flux around 50°N and 123°W in our study region. This area contains both the active volcanic belt as well as the location of significant ice mass changes. Figures 4.9a and 4.9b also show the heat flow along a profile line from the Cascadia Subduction Zone towards the North American Craton (Currie *et al.*, 2004). The spike in the heat flow around the volcanic arc is prominent, and the lower heat flow to the west, over Vancouver Island. Lithospheric thickness and asthenospheric viscosity are both temperature-controlled and would be expected to vary spatially in the study area. Figure 4.9c shows a map of lithospheric thickness inferred from studies of the wavelength of surface flexure from topography and gravity data (Currie and Hyndman, 2006). The lithosphere is thinnest along the volcanic arc and thicker around Vancouver Island. Comparing the locations of the GNSS sites used and the locations of significant ice masses to these 3 maps makes it clear that applying the same 1D earth models for the entire region would lead to some uncertainties. The GNSS sites chosen for this study may lie in areas with different lithospheric thicknesses and asthenospheric viscosities.

James *et al.* (2009) address one other issue for modelling earth rheology in the region: the fact that there is a subducting plate at various depths beneath the continental plate. James *et al.* (2009) infer a thicker lithosphere to compensate for the subducting slab, reflecting low heat flow values in the forearc

region of the subduction zone. However, the focus of this study is looking at a larger area, with a mantle wedge that increases in depth to the east. Figure 4.10 is a map showing the results of a subducting slab model with each solid contour denoting a 10 km depth difference and the short, dashed lines showing where the model contours were interpolated (McCrory et al., 2012). The slab model shown is a polynomial spline constrained by depth data from regional earthquake hypocenters, teleseismic measurements, and seismic reflection/refraction transects. Accounting for this lateral change in subducting slab depth would be necessary to increase the accuracy of the GIA models. James *et al.* (2009) found that optimal asthenospheric viscosity changed with the asthenospheric thickness. Therefore, the varied thicknesses of the mantle wedge may affect GIA response. Modelling the GIA with regards to the laterally heterogeneous lithosphere, asthenosphere, and deeper mantle in this subduction zone and arc/back arc setting warrants further study.

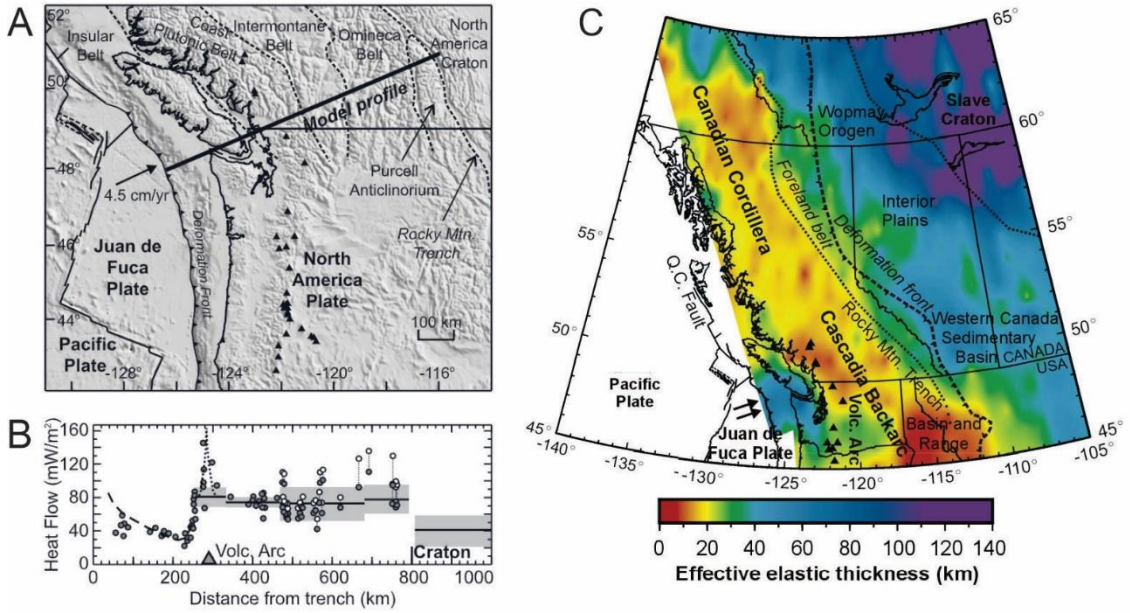

Figure 4.9*: A) a map of the heat flow model profile line from Currie et al. (2004) with B) as the plot of heat flow along that profile line, with the major heat flow spike over the volcanic arc which underlies the areas with the majority of the ice change. Adapted from Currie et al., 2004. C) is a map of Lithospheric thicknesses inferred from studies of the wavelength of surface flexure (measured from studies of topography and gravity). The thinnest (red) areas over the volcanic arc line up with b) showing the location of maximum heat flow. Adapted from Currie and Hyndman, 2006.*

In summary, the complexity of the Coast Mountains study area means that the GIA modelling conducted in this study included many assumptions and compromises. Further study using a different Earth modelling approach, such as that of finite element models for the earth's structure, would allow for considering the lateral heterogeneity of the lithospheric thickness, asthenospheric viscosity, and mantle wedge/asthenospheric thickness. Along with improved earth models, a better ice load model would explicitly incorporate glacial mass balance and flow, using a model such as OGGM, to better constrain the glacial history.

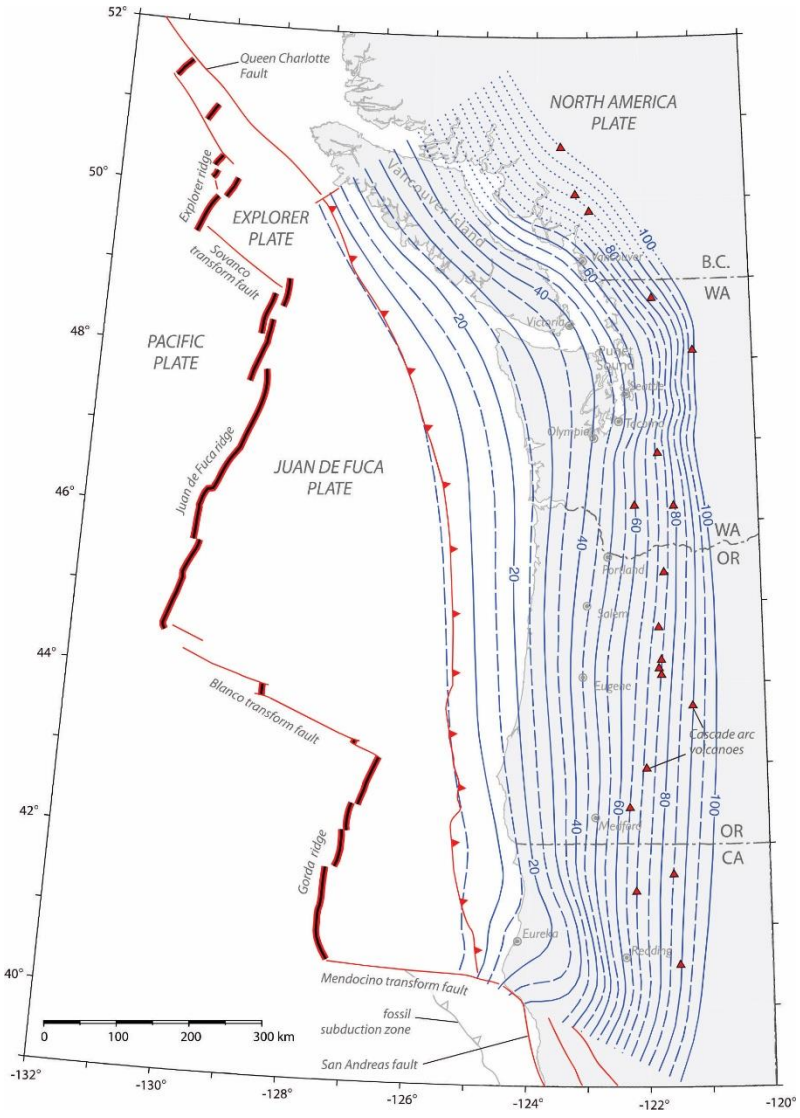

Figure 4.10*: A map of the Juan de Fuca Plate margin showing the modeled depth contours for the subducting slab. Depth contours (solid lines for every 10 km, long dashed lines for every 5 km and short dashed lines for extrapolated contours) show the depth to the Juan de Fuca slab surface. The slab descends beneath the Coast Mountains study area and could have an effect on GIA model results that the 1D earth models do not account for. Adapted from McCrory et al. 2012.*

Chapter 5: Summary and Conclusion

The objective of this study was to develop an approach to quantifying the isostatic response to LIA glacier change in the Coast Mountains of British Columbia and investigate how the response can further our understanding of the Earth's rheology through glacial isostatic adjustment (GIA) modelling. The Coast Mountains in southwestern British Columbia were selected for study for several reasons. First, the Coast Mountains have experienced significant ice mass loss since the LIA and accelerated ice mass loss in recent decades due to climate change. Second, there is information available on vertical land motion in the study area to constrain models of the GIA process. The areas of ice mass loss are located in a tectonically active region, which includes a volcanic arc. The southern portion of the study area is located in the Cascadia Subduction Zone and the northern portion is adjacent to the Queen Charlotte transform fault.

The presence of the CSZ, Queen Charlotte Fault, and Coast Range Volcanic arc all lead to the presumption of a relatively thin lithosphere and low viscosity asthenosphere, particularly when compared to Hudson Bay within the much older, stable North American Craton. The much higher heat flow and faster rates of relative sea level change of the CSZ compared to Hudson Bay suggest laterally heterogeneous Earth structure and rheology (Hyndman and Lewis, 1995). Previous studies in the CSZ have come to similar conclusions of thin lithosphere and low viscosity asthenosphere, which, when coupled with the recent ice mass loss, raise the possibility of a significant GIA response in the region from recent ice mass change following the LIA (James *et al*., 2000; 2005; 2009a; 2009b; Clague and James, 2002; Yousefi *et al*., 2018).

The GIA models in this study explore a wide range of values for Earth rheological parameters (asthenospheric viscosity and effective elastic thickness) that are then constrained through comparison to observations of vertical land motion in the region. Available GNSS vertical velocity data are compared

to the model predicted uplift rates. Seven GNSS sites in southwestern BC were chosen based on their proximity to the Coast Mountain range, the probable absence of substantial interseismic or postseismic vertical signal, and antenna monuments located on bedrock. The chosen sites were from a combination of WCDA and BCACS GNSS stations and their data were analyzed using the GIPSY 6.4 software following the Precise Point Positioning processing strategy outlined in Jiang *et al.* (2012).

Two different ice load history approaches, simulating changes in the surface loading as the glacial ice mass fluctuates over time, were employed. The ice loading history is based on gridded estimates of present-day ice thicknesses for all glaciers in the region (Farinotti et al., 2019). Ice Load A used a simple uniform thickness change profile over 3 time-steps based on extrapolated modern melt rates: 1000 CE where glacier volume is assumed to be equivalent to present-day, 1700 CE as the LIA maximum, and the present. Ice Load B is more complex and utilized a published profile of glacier change through time to create 17 time-steps for a more robust volume change history with the LIA maximum around 1700 CE (Figure 3.6). The LIA maximum volumes were determined by applying a volume-area scaling relationship (Bahr *et al*., 1997) to LIA areas from Garibaldi Park glaciers. As there is uncertainty in the values for the coefficients in the volume-area scaling relationship, a range of both c (the multiplicative scaling factor) and γ (the volume-area scaling exponent) were used to create 20 ice load histories. This allowed for a range of ice change magnitudes to be tested.

Both Ice Load A and each iteration of Ice Load B loaded 715 Earth models with density and elastic parameter structure based on the spherically symmetric PREM Earth model (Dziewonski and Anderson, 1981). Their viscosity structure is based on VM5a for the transition zone and lower mantle, but with a range of values for lithospheric thickness and asthenospheric viscosity. Lithospheric thicknesses were varied between 10 km and 110 km, and asthenospheric viscosity is varied between 1×10^{17} and 5×10^{21} Pa s, creating the 715 Earth models. GIA induced vertical velocity was predicted for each of the 715 Earth models combined with every ice load iteration (Ice Load A and 20 variants of Ice Load B). The

goodness of fit for the modeled velocities compared to the observed velocities was calculated using a normalized RMS statistic.

A general feature of the predicted uplift rates is that a thicker lithosphere distributes the uplifts over a larger area, and a higher viscosity asthenosphere generates smaller peak uplift rates. The 715 Earth models tested for Ice Load A found a best fitting lithospheric thickness of 50 km and an asthenospheric viscosity of 2×10^{19} Pa s, with an NRMS fit of 7.5 (Figure 4.4).

The more complex ice loading history for Ice Load B led to smaller (better) NRMS fits for all of the c and γ pairs, with the 9 best-fitting models having NRMS values below 6. These 9 best fitting models have lithospheric thicknesses from 45 km to 55 km and asthenospheric viscosities between 6×10^{18} Pa s and 3×10^{19} Pa s (Figure 4.4 and 4.5). Higher values of both c and γ correspond to higher values for the maximum ice volume. There is a clear trend in ice load models with larger maximum volumes leading to preferred Earth models with larger asthenospheric viscosities. The trend is less clear for lithospheric thickness; however, the only way to fit a lithospheric thickness above 45 km is to have significantly higher maximum ice volumes. As the NRMS fits were between 5.5 and 8 there are likely systematic model mismatches or the GNSS vertical velocity uncertainties are too optimistic (or a combination of the two).

One attempt to address these high NRMS values was through adjusting the observational data for two possible non-LIA GIA signals. Ice Load B model predictions were compared to a set of corrected GNSS vertical velocity observations. The corrections were done to accommodate the Yousefi *et al.* (2020) modelled interseismic uplift, as well as an assumed residual GIA signal from the retreat of the Cordilleran Ice Sheet. The corrections did not improve the NRMS fit, although they lowered the lithospheric thickness range to be between 40 km and 45 km, and the asthenospheric viscosity range from 5×10^{18} to 2×10^{19} Pa s.

Figure 5.1 compares the inferred lithospheric thickness and asthenospheric viscosity with past GIA modelling in this region, as well as GIA modelling from other tectonically active areas. The asthenospheric viscosity results from this study overlap with all the ranges found in the previous studies while lithospheric thicknesses agree with some past studies (Yousefi *et al.* (2018) for the CSZ and Hu and Freymueller (2018) for southeastern Alaska).

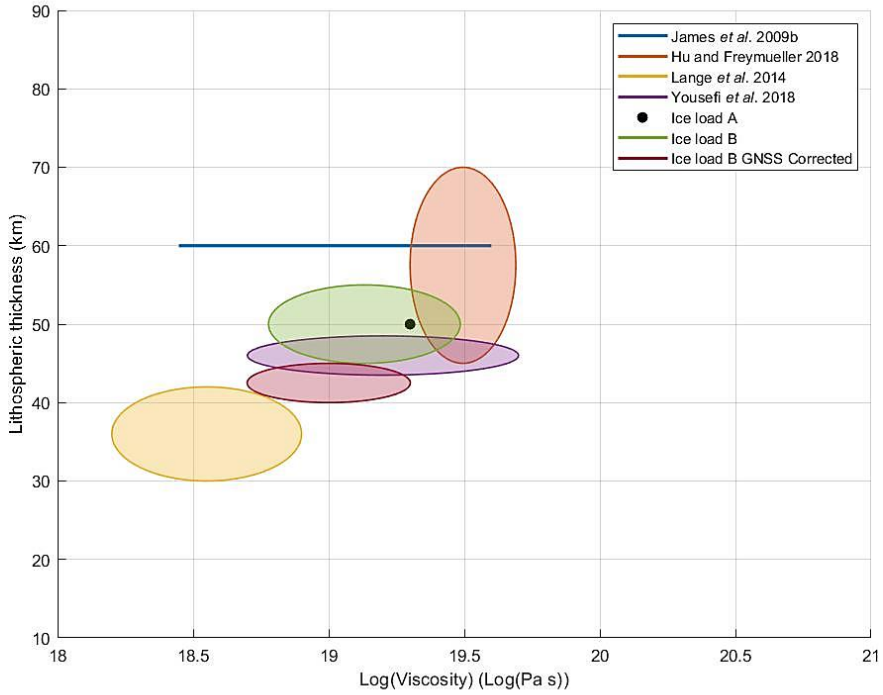

Figure 5.1: *Plot of Lithospheric thickness versus log(viscosity) ranges found by previous studies on GIA in southwestern BC area (blue line, James et al. 2009b and purple, Yousefi et al. 2018), the adjacent area of Southeast Alaska/northwestern coastal BC (orange, Hu and Freymueller 2018), and the tectonically similar Patagonia region (yellow, Lange et al. 2014). For comparison, the best fitting parameter set for Ice load A (black dot) and the parameter range for both the uncorrected (green) and corrected (dark red) Ice load B are also plotted.*

The results of this study generally agree well with previous work and the current understanding of the Coast Mountains region. Improvements to the ice load histories, earth models, and observational GNSS network could refine the constraints on Earth rheology. The Coast Mountains likely have a low asthenospheric viscosity and a thin lithosphere resulting in significant GIA response from the ice mass loss since the LIA. These results can be used to guide further work on GIA in the region and improve

understanding of lateral heterogeneity in the rheology of the Earth. GIA in the Coast Mountains will also affect relative sea level changes in the area. This needs to be assessed in order to understand local hazards that could affect coastal populations in BC, including major population centres. The results of this study can inform a future round of sea-level projections for the region as ice mass loss continues in the Coast Mountains.

References

Adhikari, S. and Marshall, S.J., 2012. Glacier volume-area relation for high-order mechanics and transient glacier states. *Geophysical Research Letters*, 39(16), p.16505.

Province of British Columbia, 2016. *B.C. Active Control System (BCACS) - Province of British Columbia*. Retrieved from: https://www2.gov.bc.ca/gov/content/data/geographic-data-services/geo-spatial-referencing/bcacs/active-control-points.

Bahr, D.B., Meier, M.F. and Peckham, S.D., 1997. The physical basis of glacier volume-area scaling. *Journal of Geophysical Research: Solid Earth*, 102(B9), pp.20355–20362.

Bahr, D.B., Pfeffer, W.T. and Kaser, G., 2015. A review of volume-area scaling of glaciers. *Reviews of Geophysics*, 53(1), pp.95–140.

Barrie, J.V. and Conway, K.W., 1999. Late Quaternary glaciation and postglacial stratigraphy of the northern Pacific margin of Canada. *Quaternary Research*, 51(2), pp.113–123.

Bevis, M., Wahr, J., Khan, S.A., Madsen, F.B., Brown, A., Willis, M., Kendrick, E., Knudsen, P., Box, J.E., Van Dam, T., Caccamise, D.J., Johns, B., Nylen, T., Abbott, R., White, S., Miner, J., Forsberg, R., Zhou, H., Wang, J., Wilson, T., Bromwich, D. and Francis, O., 2012. Bedrock displacements in Greenland manifest ice mass variations, climate cycles and climate change. Proceedings of the National Academy of Sciences of the USA, 109(30), pp.11944–11948.

Church, M. and Ryder, J., 2010. Physiography of British Columbia. In: K.D. Pike, R.G., Redding, T.E., Moore, R.D., Winkler, R.D. and Bladon, eds. 2010, *Compendium of Forest Hydrology and Geomorphology in British Columbia*. Victoria: Forest Science Program / FORREX.pp.17–46.

Cianetti, S., Giunchi, C. and Spada, G., 2002. Mantle viscosity beneath the Hudson Bay: An inversion based on the Metropolis algorithm. *Journal of Geophysical Research: Solid Earth*, 107(B12), p.ETG 12-1-ETG 12-15.

Clague, J.J. and James, T.S., 2002. History and isostatic effects of the last ice sheet in southern British Columbia. *Quaternary Science Reviews*, 21(1–3), pp.71–87.

Clague, J.J., Mathews, W.H., Ryder, J.M., Hughes, O.L., Rutter, N.W., Jackson, L.E., Matthews, J.V. and MacDonald, G.M., 1989. Quaternary Geology of the Canadian Cordillera. In: R.J. Fulton, ed. *Quaternary Geology of Canada and Greenland*. Geological Survey of Canada; Geology of Canada, Geological Society of America; Geology of North America, K-1.pp.15–96.

Clague, J.J., Menounos, B., Osborn, G., Luckman, B.H. and Koch, J., 2009. Nomenclature and resolution in Holocene glacial chronologies. *Quaternary Science Reviews*, 28(21–22), pp.2231–2238.

Clague, J.J. and Ward, B., 2011. *Pleistocene glaciation of british columbia*. In: Ehlers, J. Gibbard, P., Hughes, P., eds. *Developments in Quaternary Science, Volume 15: Quaternary Glaciations - Extent and Chronology - A Closer Look*. pp. 563-573

Currie, C.A. and Hyndman, R.D., 2006. The thermal structure of subduction zone back arcs. *Journal of Geophysical Research: Solid Earth*, 111(8), B08404.

Currie, C.A., Wang, K., Hyndman, R.D. and He, J., 2004. The thermal effects of steady-state slab-driven mantle flow above a subducting plate: The Cascadia subduction zone and backarc. *Earth and Planetary Science Letters*, 223(1–2), pp.35–48.

Darvill, C.M., Menounos, B., Goehring, B.M., Lian, O.B. and Caffee, M.W., 2018. Retreat of the Western Cordilleran Ice Sheet Margin During the Last Deglaciation. *Geophysical Research Letters*, 45(18), pp.9710–9720.

DeBeer, C.M. and Sharp, M.J., 2007. Recent changes in glacier area and volume within the southern Canadian Cordillera. *Annals of Glaciology*, 46, pp.215–221.

Desloges, J.R. and Ryder, J.M., 1990. Neoglacial history of the Coast Mountains near Bella Coola, British Columbia. *Canadian Journal of Earth Sciences*, 27(2), pp.281–290.

Dietrich, R., Ivins, E.R., Casassa, G., Lange, H., Wendt, J. and Fritsche, M., 2010. Rapid crustal uplift in Patagonia due to enhanced ice loss. *Earth and Planetary Science Letters*, 289(1–2), pp.22–29.

Dziewonski, A.M. and Anderson, D.L., 1981. Preliminary reference Earth model. *Physics of the Earth and Planetary Interiors*, 25(4), pp.297–356.

Eis, J., Maussion, F. and Marzeion, B., 2019. Initialization of a global glacier model based on present-day glacier geometry and past climate information: An ensemble approach. *Cryosphere*, 13(12), pp.3317–3335.

Farinotti, D., Huss, M., Fürst, J.J., Landmann, J., Machguth, H., Maussion, F. and Pandit, A., 2019. A consensus estimate for the ice thickness distribution of all glaciers on Earth. *Nature Geoscience*, 12(3), pp.168–173.

Gabrielse, H. (Comp.), 1991. Structural Styles. In: H. Gabrielse and C.J. Yorath, eds. *Geology of the Cordilleran Orogen in Canada*, 4th ed. Geological Society of America.pp.573–675.

Gower, J., 2017. Cryosat-2 altimetry of BC Coastal Mountain glaciers. *Remote Sensing Letters*, 8(1), pp.21–28.

Hu, Y. and Freymueller, J.T., 2019. Geodetic Observations of Time-Variable Glacial Isostatic Adjustment in Southeast Alaska and Its Implications for Earth Rheology. *Journal of Geophysical Research: Solid Earth*, 124(9), pp.9870–9889.

Hutchinson, I., James, T., Clague, J., Barrie, J.V. and Conway, K., 2004. Reconstruction of late Quaternary sea-level change in southwestern British Columbia from sediments in isolation basins. *Boreas*, 33(3), pp.183–194.

Hyndman, R.D., Currie, C.A. and Mazzotti, S.P., 2005. Subduction zone backarcs, mobile belts, and orogenic heat. *GSA Today*, 15(2), pp.4–10.

Hyndman, R.D. and Lewis, T.J., 1995. Review: the thermal regime along the southern Canadian Cordillera Lithoprobe corridor. *Canadian Journal of Earth Sciences*, 32(10), pp.1611–1617.

James, T.S. and Ivins, E.R., 1998. Predictions of Antarctic crustal motions driven by present-day ice sheet evolution and by isostatic memory of the Last Glacial Maximum. *Journal of Geophysical Research: Solid Earth*, 103(3), pp.4993–5017.

James, T.S., Clague, J.J., Wang, K. and Hutchinson, I., 2000. Postglacial rebound at the northern Cascadia subduction zone. *Quaternary Science Reviews*, 19(14–15), pp.1527–1541.

James, T.S., Hutchinson, I. and Clague, J.J., 2002. Improved relative sea-level histories for Victoria and Vancouver, British Columbia, from isolation-basin coring. *Geological Survey of Canada, Current Research 2002-A16*, p.1-7.

James, T.S., Hutchinson, I., Barrie, J.V., Conway, K.W. and Mathews, D., 2005. Relative sea-level change in the Northern Strait of Georgia, British Columbia. *Geographie Physique et Quaternaire*, 59(2–3), pp.113–127.

James, T., Gowan, E.J., Hutchinson, I., Clague, J.J., Barrie, J.V. and Conway, K.W., 2009a. Sea-level change and paleogeographic reconstructions, southern Vancouver Island, British Columbia, Canada. *Quaternary Science Reviews*, 28(13–14), pp.1200–1216.

James, T.S., Gowan, E.J., Wada, I. and Wang, K., 2009b. Viscosity of the asthenosphere from glacial isostatic adjustment and subduction dynamics at the northern Cascadia subduction zone, British Columbia, Canada. *Journal of Geophysical Research: Solid Earth*, 114(4), B04405.

Jiang, Y., Lu, Y. and Nykolaishen, L., 2021. Crustal Deformation of the 2012 Haida Gwaii Earthquake Recorded by Continuous and Episodic GPS Ground Stations in Western Canada; *Geological Survey of Canada,* Open File (under review)

Jiang, Y., Wu, X., van den Broeke, M.R., Kuipers Munneke, P., Simonsen, S.B., van der Wal, W. and Vermeersen, B.L., 2021b. Assessing Global Present-Day Surface Mass Transport and Glacial Isostatic Adjustment From Inversion of Geodetic Observations. *Journal of Geophysical Research: Solid Earth*, 126(5), e2020JB020713.

Klos, A., Bos, M.S. and Bogusz, J., 2018. Detecting time-varying seasonal signal in GPS position time series with different noise levels. GPS Solutions, 22(1), pp.1–11.

Koch, J., Clague, J.J. and Osborn, G.D., 2007a. Glacier fluctuations during the past millennium in Garibaldi Provincial Park, southern Coast Mountains, British Columbia. *Canadian Journal of Earth Sciences*, 44(9), pp.1215–1233.

Koch, J., Menounos, B. and Clague, J.J., 2009. Glacier change in Garibaldi Provincial Park, southern Coast Mountains, British Columbia, since the Little Ice Age. *Global and Planetary Change*, 66(3–4), pp.161–178.

Koch, J., Osborn, G.D. and Clague, J.J., 2007b. Pre-'Little Ice Age' glacier fluctuations in Garibaldi Provincial Park, Coast Mountains, British Columbia, Canada. *Holocene*, 17(8), pp.1069–1078.

Lange, H., Casassa, G., Ivins, E.R., Schröder, L., Fritsche, M., Richter, A., Groh, A. and Dietrich, R., 2014. Observed crustal uplift near the Southern Patagonian Icefield constrains improved viscoelastic Earth models. *Geophysical Research Letters*, 41(3), pp.805–812.

Luthcke, S.B., Arendt, A.A., Rowlands, D.D., McCarthy, J.J. and Larsen, C.F., 2008. Recent glacier mass changes in the Gulf of Alaska region from GRACE mascon solutions. *Journal of Glaciology*, 54(188), pp.767–777.

Mao, A., Harrison, C.G.A. and Dixon, T.H., 1999. Noise in GPS coordinate time series. *Journal of Geophysical Research: Solid Earth*, 104(B2), pp.2797–2816.

Mathews, W.H., 1991. Chaptre 11: Physiographic Evolution of the Canadian Cordillera. In: H. Gabrielse and C.J. Yorath, eds. 1991, *Geology of the Cordilleran Orogen in Canada*. Geological Survey of Canada, Geology of Canada Series no. 4, pp.405–418.

Maussion, F., Butenko, A., Champollion, N., Dusch, M., Eis, J., Fourteau, K., Gregor, P., Jarosch, A.H., Landmann, J., Oesterle, F., Recinos, B., Rothenpieler, T., Vlug, A., Wild, C.T. and Marzeion, B., 2019. The Open Global Glacier Model (OGGM) v1.1. *Geoscientific Model Development*, 12(3), pp.909–

931.

McCrory, P.A., Blair, J.L., Waldhauser, F. and Oppenheimer, D.H., 2012. Juan de Fuca slab geometry and its relation to Wadati-Benioff zone seismicity. *Journal of Geophysical Research: Solid Earth*, 117(9), B09306.

Menounos, B., Hugonnet, R., Shean, D., Gardner, A., Howat, I., Berthier, E., Pelto, B., Tennant, C., Shea, J., Noh, M.J., Brun, F. and Dehecq, A., 2019. Heterogeneous Changes in Western North American Glaciers Linked to Decadal Variability in Zonal Wind Strength. *Geophysical Research Letters*, 46(1), pp.200–209.

Menounos, B., Koch, J., Osborn, G., Clague, J.J. and Mazzucchi, D., 2004. Early Holocene glacier advance, southern Coast Mountains, British Columbia, Canada. *Quaternary Science Reviews*, 23(14–15), pp.1543–1550.

Menounos, B., Osborn, G., Clague, J.J. and Luckman, B.H., 2009. Latest Pleistocene and Holocene glacier fluctuations in western Canada. *Quaternary Science Reviews*, 28(21–22), pp.2049–2074.

Mitrovica, J.X. and Peltier, W.R., 1992. Constraints on mantle viscosity from relative sea level variations in Hudson Bay. *Geophysical Research Letters*, 19(12), pp.1185–1188.

NRCan, 2018. *Canadian Active Control System (CACS)*. National Resources Canada. Retrieved from: https://webapp.geod.nrcan.gc.ca/geod/data-donnees/cacs-scca.php?locale=en

Nykolaishen, L., Dragert, H., Wang, K., James, T.S. and Schmidt, M., 2015. GPS observations of crustal deformation associated with the 2012 Mw 7.8 Haida Gwaii earthquake. *Bulletin of the Seismological Society of America*, 105(2B), pp.1241–1252.

Peltier, R., Argus, D. and Drummond, R., 2013. The new ICE-6G (VM5a) model of the Global Process of Glacial Isostatic Adjustment. *JGR: Solid Earth*, 15, p.6299.

Peltier, W.R., 2004. Global glacial isostasy and the surface of the ice-age earth: The ICE-5G (VM2) Model and GRACE. *Annual Review of Earth and Planetary Sciences*, 32(1), pp.111–149.

Peltier, W.R., Argus, D.F. and Drummond, R., 2015. Space geodesy constrains ice age terminal deglaciation: The global ICE-6G-C (VM5a) model. *Journal of Geophysical Research: Solid Earth*, 120(1), pp.450–487.

Porritt, R.W., Miller, M.S. and Darbyshire, F.A., 2015. Lithospheric architecture beneath Hudson Bay. *Geochemistry, Geophysics, Geosystems*, 16(7), pp.2262–2275.

Roy, K. and Peltier, W.R., 2018. Relative sea level in the Western Mediterranean basin: A regional test of the ICE-7G_NA (VM7) model and a constraint on late Holocene Antarctic deglaciation. *Quaternary Science Reviews*, 183, pp.76–87.

Ryder, J.M., Fulton, R.J. and Clague, J.J., 1991. The Cordilleran Ice Sheet and the glacial geomorphology of southern and central British Columbia. *Geographie Physique et Quaternaire*, 45(3), pp.365–377.

Ryder, J.M. and Thomson, B., 1986. Neoglaciation in the southern Coast Mountains of British Columbia: chronology prior to the late Neoglacial maximum. *Canadian Journal of Earth Sciences*, 23(3), pp.273–287.

Schiefer, E., Menounos, B. and Wheate, R., 2007. Recent volume loss of British Columbian glaciers, Canada. *Geophysical Research Letters*, 34(16).

Shapiro, N.M., Ritzwoller, M.H., Mareschal, J.C. and Jaupart, C., 2004. Lithospheric structure of the Canadian Shield inferred from inversion of surface-wave dispersion with thermodynamic a priori constraints. *Geological Society Special Publication*, 239, pp.175–194.

Shugar, D.H., Walker, I.J., Lian, O.B., Eamer, J.B.R., Neudorf, C., McLaren, D. and Fedje, D., 2014. Post-glacial sea-level change along the Pacific coast of North America. *Quaternary Science Reviews*, 97, pp.170–192.

Stumpf, A.J., Broster, B.E. and Levson, V.M., 2000. Multiphase flow of the late Wisconsinan Cordilleran ice sheet in Western Canada. *Bulletin of the Geological Society of America*, 112(12), pp.1850–1863.

Turcotte, D. and Schubert, J., 2002. *Geodynamics*. 2nd ed. Cambridge, UK: Cambridge University Press.

VanLooy, J.A. and Forster, R.R., 2008. Glacial changes of five southwest British Columbia icefields, Canada, mid-1980s to 1999. *Journal of Glaciology*, 54(186), pp.469–478.

Wada, Y., Van Beek, L.P.H., Sperna Weiland, F.C., Chao, B.F., Wu, Y.H. and Bierkens, M.F.P., 2012. Past and future contribution of global groundwater depletion to sea-level rise. Geophysical Research Letters, 39(9).

Wessel, P., Smith, W.H.F., Scharroo, R., Luis, J. and Wobbe, F., 2013. Generic Mapping Tools: Improved Version Released. *Eos, Transactions American Geophysical Union*, 94(45), pp.409–410.

Yousefi, M., Milne, G., Li, S., Wang, K. and Bartholet, A., 2020. Constraining interseismic deformation of the Cascadia subduction zone: New insights from estimates of vertical land motion over different timescales. *Journal of Geophysical Research: Solid Earth*, 125(3), p.e2019JB018248.

Yousefi, M., Milne, G.A., Love, R. and Tarasov, L., 2018. Glacial isostatic adjustment along the Pacific coast of central North America. *Quaternary Science Reviews*, 193, pp.288–311.

Zumberge, J.F., Heflin, M.B., Jefferson, D.C., Watkins, M.M. and Webb, F.H., 1997. Precise point positioning for the efficient and robust analysis of GPS data from large networks. *Journal of Geophysical Research: Solid Earth*, 102(B3), pp.5005–5017.